The effect of photoionisation feedback on star formation in giant molecular clouds

(分子雲における輻射が星形成に与える影響)

Kazuhiro Shima (島 和宏)
Department of Cosmosciences, Graduate School of Science,
Hokkaido University

March 2018

Abstract

Stars form from collapsing cold molecular clouds (GMCs) and can change the physical state of the parent cloud by emitting energy into its surrounding environment. The energy will stop or improve the future star formation by destroying the cloud or triggering stars. Understanding the processes of star formation and the interplay with the parent cloud is therefore very important in astrophysics.

The star formation and the effect of feedback should depend on the cloud internal properties. Clouds are turbulent and not uniform gas distributions which leads to multiple star formation sites. The local conditions of the gas around the star formation site can play a key role in determining the star formation. High-density regions that could not be dispersed are then heated by feedback to increase the Jeans mass and lead to more massive star formation. Alternatively, lower density regions could be blown out by feedback, ending the star formation. I focused on how the feedback effect depends on the initial cloud structures. I considered idealised and non-idealised sets of initial conditions and investigated the total effect of feedback on the star formation history.

[1] Does feedback help or hinder star formation? The effect of photoionization on star formation in giant molecular clouds (Shima et al. 2017a)

I investigated the effect of photoionising feedback both inside idealised and inside more realistic cloud structures extracted from a global galaxy simulation. I showed that feedback can both promote and suppress star formation in the idealised case. On the other hands, star formation is suppressed by feedback in the extracted case because the gas has fragmented into small dense cores by global galaxy tidal interactions and the structures are unaffected by the injection of radiation energy. Instead, the collapse was slowed to reduce the star formation efficiency.

[2] The effect of photoionizing feedback on star formation in isolated and colliding clouds (Shima et al. 2017b)

I perfomed hydrodynamical simulations of self-gravitating turbulent gas including photoionising feedback and investigate star formation occurring in giant molecular clouds, comparing structures that evolve in isolation versus those produced during a cloud collision. Observational evidence strongly suggests that colliding objects promote the production of massive stars in

a short timescale by compressing gas at the interface of the two colliding clouds. Two different collision speeds are investigated and the impact of photoionising radiation from the stars is determined. I find that a colliding system leads to more massive star formation both with and without the addition of feedback, raising overall star formation efficiencies (SFE) by a factor of 10 and steepening the high-mass end of the stellar mass function. This rise in SFE is due to increased turbulent compression during the cloud collision. While feedback can both promote and hinder star formation in the isolated system, it increases the SFE by approximately 1.5 times in the colliding case when the thermal speed of the resulting H II regions matches the shock propagation speed in the collision.

Contents

Chapter 1

Introduction

In the interstellar medium (ISM), stars form from the gravitational collapse of the coldest part of molecular gas that are identified as the giant molecular clouds (GMCs). Observations of nearby galaxies have shown that there is a strong correlation between the molecular gas density and star formation (Bigiel et al. 2011). The correlation proposes that GMCs are forming stars in a similar manner in different galaxies. It is therefore very important to investigate how gas is converted into stars. However, the pc-scale physical processes driving star formation inside GMCs are unclear and poorly understood because they are non-linear and complex.

What happens to the cloud with feedback is also a topic of intense debate. Sufficiently strong feedback must have negative effect in the sense of disrupting the cloud entirely and ending all prospects of future star formation (Murray 2011). One notch down would see the cloud significantly damaged, delaying the onset of a second generation of stars (Williamson et al. 2014; Meidt et al. 2015; Tasker et al. 2015). To explain the observed low SFR, feedback should have negative effect and regulate star formation. However, it is not necessarily that each feedback has always negative effect. The effect of feedback might be positive in the sense of enhancing or triggering new star formation. While feedback drives gas away from the star formation site, the outer edge of the resulting expanding shell can fragment into a population of triggered stars (Whitworth et al. 1994; Wünsch et al. 2010; Koenig et al. 2012). Alternatively, heat from the newly forming stars can increase the local Jeans mass, reducing the gas fragmentation to produce more massive stars in place of a large number of smaller objects (Bate 2009; Offner et al. 2009; Urban et al. 2010).

The impact of feedback should depend on the cloud properties. The mass

and radius of a cloud controls its escape velocity; a value that affects the extent outflows can travel. Dale et al. (2014) found that H II regions played the dominant effect for small clouds with a lower escape velocity than 10 km s^{-1}. On the other hand they has little impact for clouds with higher escape velocities. More compact clouds will have a higher surface density, allowing radiation to be more efficiently trapped with the cloud where it can have a stronger effect. Krumholz et al. (2010) found that a high surface density allowed high accretion rates for the forming protostars, whose radiation from the accretion luminosity was then trapped in the dense cloud.

The differences do not stop with the global cloud properties. Clouds are not uniform gas distributions that form stars only within a dense central region. Rather, they are turbulent, irregular bodies that can harbour a large multiple of star formation sites (Larson 1981). This means that the local conditions of the gas around the star formation site are a long way from being a homogeneous pool and these small-scale variations can play a key role. Heat that is deposited into dense gas will cool rapidly, reducing the region affected by that feedback. On the other hand, if stars form near pockets of low density gas, then the energy may have a much longer-range impact. Comparing observations of wind blown bubbles around stellar clusters with theoretical models, Harper-Clark & Murray (2009) found that a non-homogeneous medium is needed to match observations, which allows energy to leak through the bubble shell.

All this points to an efficiency for feedback that may come down less to the feedback itself and more to the structure of the cloud. It must therefore be important to determin cloud properties affecting the evolution and the rate of conversion from gas into stars. Howerver, if cloud structure is the key, how can this be included self-consistently in feedbcak modelss? Observations outside the Milky Way can now estimate the bulk properties of individual clouds, but not yet map their interior dynamics (Hughes et al. 2013; Donovan Meyer et al. 2013). Simulations suffer from similar problems, with those modelling the global galaxy disc creating self-consistent gas profiles but being unable to resolve the cloud interior, or alternatively following the gas inside the cloud but using an idealised initial set-up (Federrath et al. 2014; Offner & Krumholz 2009).

The properties of clouds have been shown to strongly depend on their galactic environment, with disc shear, grand design structrue and nieghbouring cloud interactions sculpting their evolution. In global simulations with and without star formation and thermal feedback, Tasker et al. (2015) found that cloud properties were not strongly dependent on internal processes, supporting the idea that cloud evolution can also be driven by ex-

ternal conditions. Insimilar simulations without star formation, Jin et al. (2017) found a wide range of turbulence modes were created within clouds due to their mutual interaction within the galactic disc. Such global-scale interference is supported by observations that see variations in GMCs and specific star formation rates within different galactic structures (Koda et al. 2009; Meidt et al. 2013; Momose et al. 2010).

In Chapter 3, I investigate the effect of photoionising feedback on the star formation within a giant molecular cloud. I look at two sets of cloud models. In the first, the cloud is modelled as an idealised turbulent sphere of gas. I compare the effects of star formation with no form of feedback with the changes when stars radiate and finally when old stars explode as supernovae, depositing thermal energy into the gas. In the second cloud model, the cloud is extracted from a global galaxy simulation. I compare the resulting evolution with star formation only and when including phtoionisation. This is one way to try and bridge the two scales by using properties derived from a global simulation as the initial starting point for a smaller-scale model. Where this has been done, the importance of the gas structure has become clear. On parsec-scales within a single GMC clump whose structure is taken from numerical models, Rogers & Pittard (2013) looked at effect of wind-driven bubbles. They found that the variations in gas structure allowed hot, high speed gas to escape long low density channels, producing a strongly different effect from a uniform density environment. The energy from the final supernovae explosion largely escapes the now fractured gas shell. On slightly larger scales, Rey-Raposo et al. (2015) compared the evolution and star formation of clouds extracted from a global galaxy simulation with those modelled as idealised turbulent spheres. While their models did not include feedback, they found that the differing velocity structures in the clouds produced very different evolutions. The sphere evolution was governed principally by gravitationally infall, while the extracted clouds had a more involved velocity structure from the galactic disc sheer.

Another intersting process affecting the evolution of GMCs is cloud-cloud collision. Fujimoto et al. (2014a) found global structures such as spiral arms and a galactic bar could change the range in cloud properties by increasing the rate of cloud-cloud interactions.

Much speculation surrounds the role of such collisions between the GMCs for massive star formation. Massive stars and clusters are difficult to form through isolated gravitational collapse, since the formation of massive stars should heat the local environment and prevent further accretion (acting as a cap on maximum star size) and disperse the surrounding gas. During a collision, gas is compressed at the interface between the two clouds, creating

a high density shell of gas. The rise in density can potentially reduce the local Jeans mass to lead to a lower characteristic stellar mass (Hennebelle & Chabrier 2009), but the collision can also promote the production of massive stars from an increase in the velocity dispersion or a faster formation timescale that allows longer accretion from the surrounding dense gas. If such collisions can be interpreted as compressive driving of turbulence, then we expect an enhanced star formation rate by factors ranging from a few to up to 10 (Federrath & Klessen 2012; Federrath et al. 2016)

Which processes dominate GMC evolution may be reflected in the resulting star formation. If collision processes are the key component to dictating a cloud's star formation history, then the stellar population may principally may be created in the collision events. Observations have also supported the notion that cloud interactions are common events. Super star clusters with masses $\sim 10\,M_{\odot}$ packed into a cluster of radius$\sim 1\,$pc have been observed to be associated with clouds colliding at velocities around 10–20 km s^{-1} (Furukawa et al. 2009; Ohama et al. 2010; Fukui et al. 2016), as well as sites of high-mass star formation (Torii et al. 2015). In simulations of colliding clouds between 7–15 pc in size, Takahira et al. (2014) found that collisions produced massive star-forming cores and a playoff took place between the shock speed which heightened core production and the duration of the shock moving within the cloud, which allowed cores to grow within the dense environment. Parsec-scale clouds in simulations by Balfour et al. (2015; 2017) agreed that the slower collisions were more efficient at forming massive stars in these smaller systems, while Wu et al. (2017) confirmed a star formation rate and efficiency higher by a factor of ten in colliding GMCs with added support from magnetic fields. Ultimately, these results agree that if cloud evolution is driven by collisional interactions and result in a tendency towards more massive stars, then the resulting stellar initial mass function (IMF) should be more top-heavy than if the cloud evolved in isolation.

In Chapter 4, I explore the star formation from isolated and colliding GMCs and the evolution after energy injection by stellar feedback. Unlike previous simulations by Takahira et al. (2014) and also those considered by Wu et al. (2017), I include a sink particle method into a grid based code that allows stars to gather gravitationally bound and collapsing gas from their surrounding environment. These criteria ensure that if the turbulence is high, a higher mass will be needed for the particle creation. Therefore, an increase of turbulence within the shock will lead to more massive stars. I also include output feedback energy from photoionisation.

1.1 ISM physics

This section will describe briefly about important physics in the ISM.

1.1.1 Self-Gravity

We can roughly estimate the dynamical and time scale of star formation. With a uniform equilibrium gas sphere, there is a critical length known as the Jeans length for the stability against perturbations. The length (λ_J) is given by:

$$\lambda_J = \frac{c_s}{\sqrt{\rho G}}, \tag{1.1}$$

where c_s is the isothermal sound speed of the sphere, ρ is the uniform density and G is the gravitational constant. All objects larger than this scale are unstable and will collapse with the self-gravity. The mass inside the Jeans length is also often used (the Jeans mass, M_J) and it is given by:

$$M_J = \frac{4\pi}{3}\rho\left(\frac{\lambda_J}{2}\right)^3 = \frac{\pi}{6}\frac{c_s^3}{\sqrt{\rho G^3}}. \tag{1.2}$$

The time scale by free-fall gravitational collapse (t_{ff}) is given by:

$$t_{ff} = \sqrt{\frac{3\pi}{32\rho G}}. \tag{1.3}$$

The typical molecular clouds has masses of $\sim 10^2$–$10^7\,\mathrm{M}_\odot$, sizes of $\sim$1–100 pc and the average number densities of $\sim 10^3$–$10^5\,\mathrm{cm}^{-3}$. If the gas is converted into stars within the free-fall time scale, the star formation rate (SFR) would be $\sim 200\,\mathrm{M}_\odot\,\mathrm{yr}^{-1}$. However, our Milky Way only produces stars at $\sim$1–$2\,\mathrm{M}_\odot\,\mathrm{yr}^{-1}$ (Chomiuk & Povich 2011), which is about two orders of magnitude lower than the theoretically estimated value. The GMCs are therefore either unbound structures and not dominated by their gravity, or they receive additional support from sources such as turbulence, magnetic fields, and/or stellar feedback to prevent GMCs to form stars at a higher rate than observed.

1.1.2 Turbulence

Turbulence are commonly observed in molecular clouds and the random motions may prevents the global collapse regulating star formation. Larson (1981) established a power-law correlation between the internal velocity

dispersion (σ_c; the standard deviation of cloud turbulent velocities) and the cloud size (R_c),

$$\left(\frac{\sigma_c}{[\mathrm{km\,s^{-1}}]}\right) \propto \left(\frac{R_c}{[\mathrm{pc}]}\right)^{0.38}. \tag{1.4}$$

The power index is nearly 1/3, so he suggested the Kolmogrov turbulence may be the origin. The virial theorem is used to indicates whether GMCs are gravitationally bound or not. The virial parameter (α_{vir}) is given by:

$$\alpha_{\mathrm{vir}} = \frac{5\sigma_c^2 R_c}{GM_c}, \tag{1.5}$$

where M_c is the total cloud mass. Clouds with $\alpha_{\mathrm{vir}} < 2$ are supercritical and unstable to collapse. Both observations and global simulations that form clouds within a modelled galactic disc, suggest that GMCs have $\alpha_{\mathrm{vir}} \sim 1$ (Roman-Duval et al. 2010; Dobbs et al. 2011; Tasker et al. 2015; Jin et al. 2017). So clouds are bound but turbulence may delay the global collapse and star formation.

On the other hand, turbulence may enhance star formation in smaller scales. Larger clouds have a higher velocity dispersion than it's sound speed. The sound speed of isothermal ideal gas is given by

$$c_s = \sqrt{\frac{k_B T}{\mu m_H}}, \tag{1.6}$$

where k_B, T, μ and m_H are the Boltzmann constant, temperature, the mean molecular weight and the hydrogen atomic mass, respectively. For molecular gas with $\sim 10\,\%$ helium and a few metals, μ =2.7 is often used. The typical temperature of star formating dense cores is 10 K as a result of balance between heating and cooling processes. Then the sound speed is $\sim$0.2 $\mathrm{km\,s^{-1}}$ and the cloud's sonic Mach number ($\mathcal{M} = \sigma_c/c_s$) becomes lager than 1. This means the turbulence is supersonic. The supersonic flows creates shocks and induces local compression of gas.

The drivers for turbulence may be internal or external (Federrath et al. 2017). Internal drivers chiefly consist of thermal and kinetic feedback from the production of stars. This can both disrupt neighbouring collapsing regions of gas and also trigger collapse at the edge of expanding shells of hot gas. The combined pressure from feedback could eventually disrupt the cloud and throttle star formation, but if the gas was extremely dense the feedback was unable to dominate over gravity. Cloud collisions may be a external driver and produce strong compressive turbulence enhancing star formation.

1.1.3 Photoionisation

Massive stars have higher effective temperatures emitting large quantities of UV radiation. Photoionisation is caused by radiation with energy above 13.6 eV (ionisation energy for the hydrogen atom) and the over-energy heats gas to a equilibrium temperature of $\sim 10^4$ K in the ionised H II gas. The H II regions therefore are blows bubbles by the large pressure gradient between the hot gas and the surrounded cold gas. The expanding velocity is the order of the sound speed in the H II region $\sim 10\,\mathrm{km\ s^{-1}}$. The detail physical processes are described in Appendix.

1.1.4 Supernovea

Massive stars go supernovae and yields $\sim 10^{51}$ erg as thermal energy at the end of its lifetime, leaving behind neutron stars or black holes. Multiple supernova explosions will mix gas and drive galactic scale turbulence. The typical life time is $\sim 4\,\mathrm{Myr}$ for a $100\,\mathrm{M}_\odot$ star. Supernovae will destroy the cloud completely but they do not happen until at least 4 Myr after the massive star formation. Observations of 30 Doradus, which is the largest H II regions in nearby galaxies, shows that the cloud has already been affected before a supernova occurred (Lopez et al. 2011). It is important to investigate the interplay between the parent cloud and the other feedback processes before the supernova.

Chapter 2

Numerical Methods

Simulations are performed by *Enzo* (Bryan et al. 2014), a 3D Adaptive Mesh Refinement (AMR) hydrodynamics code. This section briefly describes the fundamental physics and numerical algorithms implemented into *Enzo*.

2.1 Hydrodynamics

Enzo offers magneto-hydrodynamical simulations including the cosmic expansion, but magnetic fields and a co-moving coordinate system are not assumed in this study. Then the hydrodynamics equations reflecting pressure and gravity forces are given by

$$\frac{\partial \rho}{\partial t} + \nabla \cdot (\rho \boldsymbol{v}) = 0, \tag{2.1}$$

$$\frac{\partial \rho \boldsymbol{v}}{\partial t} + \nabla \cdot (\rho \boldsymbol{v}\boldsymbol{v} + \boldsymbol{I}p) = -\rho \nabla \phi, \tag{2.2}$$

$$\frac{\partial E}{\partial t} + \nabla \cdot (E + p)\,\boldsymbol{v} = -\rho \boldsymbol{v} \cdot \nabla \phi - \Lambda + \Gamma. \tag{2.3}$$

where ρ, $\boldsymbol{v}$, p, ϕ, E, Λ and Γ are gas density, peculiar velocities, thermal pressure, gravitational potential, the total fluid energy density, cooling rate and heating rate, respectively. The matrix $\boldsymbol{I}$ is the identity matrix. The first equation represents conservation of mass, the second represents conservation of momentum, and the third represents conservation of total fluid energy. The total fluid energy density E is given by

$$E = e + \frac{\rho |\boldsymbol{v}|^2}{2}, \tag{2.4}$$

where e is thermal energy density. The equations are closed by an equation of state and the Poisson's equation for the gravitational potential:

$$e = \frac{p}{\gamma - 1}, \tag{2.5}$$

$$\nabla^2 \phi = 4\pi G \left(\rho - \rho_0\right), \tag{2.6}$$

where γ, G and ρ_0 are a ratio of specific heats, the gravitational constant and the mean density, respectively.

2.2 Adaptive Mesh Refinement

AMR is a efficient and suitable technique for astrophysical fluid simulations following the large spatial and temporal dynamical ranges with finite memory and computational time. *Enzo* solves the Eulerian equations of hydrodynamics on each cell of a mesh with a uniform Cartesian grid. The entire region is covered by the root grid and finer child meshes are added adaptively to regions where we are interested in and higher accuracy is needed. The ratio between the cell sizes of parent and child meshes is two. Each child mesh itself can become a new parent mesh for more highly refined child meshes. The refinement criteria is user selectable depending on our interests. In this study, the criteria is based on the requirement that the local Jeans length must not fall below five cells. This limit is slightly larger than the four cells per Jeans length suggested by Truelove et al. (1997) as the minimum needed to prevent spurious numerical fragmentation of turbulent gas.

2.3 Hydrodynamic Solver

Several hydrodynamic solver methods are implemented in *Enzo*. In this study, *Zeus* scheme (Stone & Norman 1992) which is a Second-order finite difference algorithm is used. The scheme is second-order accurate in space but first-order accurate in time.

The finite difference equations are solved by four steps. First, the pressure force is added:

$$v_j^{n+a} = v_j^n - \frac{\delta t}{\delta x_j} \frac{p_j^n - p_{j-1}^n}{(\rho_j^n + \rho_{j-1}^n)/2}. \tag{2.7}$$

In the *Zeus* formalism, the subscripts (j) indicate face-centered quantity for velocity and cell-centered quantities for density, pressure and energy.

Therefore, the v_j refers to the velocity at potion $x_{j-1/2}$. The superscripts indicate partial updates in time. Then, a von Neumann-Richtmyer artificial viscosity is added for the stability:

$$v_j^{n+b} = v_j^{n+a} - \frac{\delta t}{\delta x_j} \frac{q_j^{n+a} - q_{j-1}^{n+a}}{(\rho_j^n + \rho_{j-1}^n)/2}, \tag{2.8}$$

$$e_j^{n+b} = e_j^n - \frac{\delta t}{\delta x_j} q_j^{n+a} (v_{j+a}^{n+a} - v_j^{n+a}). \tag{2.9}$$

The artificial viscosity coefficient q_j is given by:

$$q_j = \begin{cases} Q_{\rm AV} \rho_j (v_{j+1} - v_j)^2, & \text{if } (v_{j+1} - v_j) < 0 \\ 0, & \text{otherwise} \end{cases} \tag{2.10}$$

where $Q_{\rm AV}$ is a constant value of two. This smoothes shock discontinuities and the scheme is more robust than others. Third, the compression term is given by

$$e_j^{n+c} = e_j^{n+b} \left(\frac{1 - (\delta t/2)(\gamma - 1)(\nabla \cdot \boldsymbol{v})_j}{1 + (\delta t/2)(\gamma - 1)(\nabla \cdot \boldsymbol{v})_j} \right). \tag{2.11}$$

The final step for conservation is given by

$$\rho_j^{n+1} = \rho_j^n - \frac{\delta t}{\delta x_j} (\rho_{j+1/2}^* v_{j+1}^{n+c} - \rho_{j-1/2}^* v_j^{n+c}). \tag{2.12}$$

Here $\rho_{j-1/2}^*$ is the correctly up-winded value at potion $x_{j-1/2}$. The velocity is a face-centered quantity and the density is a cell-centered quantity, so the mass flux at the cell boundary is given by $\rho_{j-1/2}^* v_j$.

2.4 Gravity

To calculate the accelerations due to self-gravity, the Poisson's equation is solved by a Fast Fourier Transform (FFT) technique on the root grid on each time step. The boundary conditions of sub-grids are interpolated from the root grid. The Poisson's equation is solved by using a multi-grid technique on the sub-grids at a time.

2.5 Chemistry

In this study, *Enzo* follows nine atomic and molecular species (H, H^+, He, He^+, He^{++}, e, H^-, H_2 and H_2^+) using a non-equilibrium chemical network.

The chemical processes and the rate coefficients of collisional and radiation reactions are summarized in Abel et al. (1997). The formation of H_2 on dust grains is also assumed (Omukai 2000) when temperature is below than 1500 K (dust will melt at this temperature).

2.6 Cooling and Heating

The cooling and heating rate of gas is computed from the chemical abundances with the optically thin approximation. The following processes are assumed: (1) collisional excitation cooling, (2) collisional ionisation cooling, (3) recombinations cooling, (4) bremsstrahlung cooling, (5) molecular hydrogen cooling and heating from the formation on dust grains, (6) CIE cooling, and (7) gas to dust grains heat transfer. The cooling rate equations of atomic and molecular species are summarized in Annious et al. (1997) and Omukai (2000). The importance of collision–induced emission (CIE) cooling is discussed in Ripamonti & Abel (2004). The equation of energy transfer from gas to dust grains are taken from Hollenbach & McKee (1989). Other cooling processes from metals heavier than helium is included as a function of density, metallicity and temperature. The metal cooling is based on multidimensional cooling rate tables computed with the CLOUDY code (Ferland et al. 1998; Smith et al. 2008). All simulations in this study assume the solar metallicity.

The gas is also heated by photoelectric heating from UV-irradiated dust grains. The photoelectric heating is important thermal processes at low densities (n_H <1–10^3 cm^{-3}). The heating rate is proportional to the gas density as implemented in Tasker (2011). If stellar feedback is turned on, photoelectric heating by ionisation photons is coupled. The details are described in section 2.8.

2.7 Star Formation

I developed and used several star formation models. The details are described in Chapter 3 and Chapter 4.

2.8 Radiative Transfer

If the sink particle mass exceeds 20 $M_\odot$ after the accretion has finished, the particle will emit ionising radiation. The ionising luminosity is $10^{46.85}$ ph s^{-1} $M_\odot^{-1}$, which assumes solar metallicity and a Salpeter IMF between 1–100 $M_\odot$

(Schaerer 2003). The rays are assumed to be monochromatic spectrum with a mean ionising photon energy of $E_{\rm ph} = 20.84\,{\rm eV}$. The radiative feedback is calculated by a photon-conserving radiative transfer algorithm (Abel & Wandelt 2002; Wise & Abel 2011) with adaptive ray-tracing scheme based on Hierarchical Equal Area isoLatitude Pixelation (HEALPix) framework (Górski et al. 2005).

The radiative transfer equation is given by

$$\frac{1}{c}\frac{\partial I_\nu}{\partial t} + \hat{n}\frac{\partial I_\nu}{\partial x} = -\kappa_\nu I_\nu + j_\nu, \tag{2.13}$$

where c is the speed of light, I_ν is the specific intensity of the radiation in units of energy per time per solid angle per unit area at a frequency ν, κ_ν is the absorption coefficient and j_ν is the point source of radiation emitting radial rays that are propagated along the direction $\hat{n}$. Along each monochromatic ray, the equation reduces to

$$\frac{1}{c}\frac{\partial P}{\partial t} + \frac{\partial P}{\partial r} = -\kappa P, \tag{2.14}$$

where P is the photon number flux along a ray. Photons are integrated outwards from the source.

To sample an enough number of photons at a large radius R from the source, the ray-tracing scheme requires at least 5 rays in each cell. This requirement is satisfied by the HEALPix framework. The rays at the source are equally spread across $N_{\rm pix} = 12 \times 4^1$ rays, then the ratio of the face area $A_{\rm cell}$ of a cell and the solid angle Ω_{ray} of the ray is given by

$$\Phi_c = \frac{A_{\rm cell}}{\Omega_{\rm ray}} = \frac{N_{\rm pix}(\Delta x)^2}{4\pi R_0^2}, \tag{2.15}$$

where R_0 is the distance the ray traveled and Δx is a cell width. If the Φ_c is less than 5, the ray is split into 4 child rays.

The radiative transfer equation has a simple exponential analytic solution for the monochromatic ray and the photon flux is given by,

$$dP = P \times (1 - e^{-\tau}), \tag{2.16}$$

where τ is a optical depth given by the integration of

$$d\tau = \sigma_{\rm abs} n_{\rm abs} dr. \tag{2.17}$$

Here $\sigma_{\rm abs}$ is the cross section and $n_{\rm abs}$ is number density of the absorbing medium. The photoionisation cross-sections is summarized in Annious et al. (1997). In this study, only hydrogen is assumed as the absorbing medium.

The photoionisation rates $k_{\rm ph}$ and the photo-heating rates $\Gamma_{\rm ph}$ associated with a single ray are given by

$$k_{\rm ph} = \frac{P(1-e^{-\tau})}{n_{\rm abs} V_{\rm cell} dt}, \tag{2.18}$$

$$\Gamma_{\rm ph} = k_{ph}(E_{\rm ph} - E_{\rm H}), \tag{2.19}$$

where $V_{\rm cell}$, $E_{\rm ph}$ and $E_{\rm H}$ are the cell volume, the photon energy and the ionisation energy of hydrogen, respectively. Since we ignore the radiative feedback from sink particles below $20\,{\rm M}_\odot$ for computational reasons, our feedback can be considered a lower limit.

Chapter 3

Does feedback help or hinder star formation?

3.1 Abstract

I investigated the effect of photoionising feedback inside turbulent star-forming clouds, comparing the resultant star formation in both idealised profiles and more realistic cloud structures drawn from a global galaxy simulation. I performed a series of numerical simulations which compared the effect of star formation alone, photoionisation and photoionisation plus supernovae feedback. In the idealised cloud, photoionisation suppresses gas fragmentation at early times, resulting in the formation of more massive stars and an increase in the star formation efficiency. At later times, the dispersal of the dense gas causes the radiative feedback effect to switch from positive to negative as the star formation efficiency drops. In the cloud extracted from the global simulation, the initial cloud is heavily fragmented prior to the stellar feedback beginning and is largely structurally unaffected by the late injection of radiation energy. The result is a suppression of the star formation. I conclude that the efficiency of feedback is heavily dependent on the gas structure, with negative feedback dominating when the density is high.

3.2 Numerical methods

In this section, I will describe the specific methods for my feedback models. For the idealised cloud simulations, the box size has a side of 200 pc, covered by a 128^3 root grid and an additional two static meshed corresponding

to a minimum 512^3 resolution over the cloud. An additional three levels of adaptive refinement were included, with each static and adaptive mesh reducing the cell size by a factor of two. This gave a limited resolution of 0.05 pc. I performed two additional high-resolution simulations (with and without photoionising radiation) that reduced the cell size by a further factor of two. For the simulation that used the extracted cloud, the box size was larger with side 500 pc. This was on a 64^3 root grid which corresponded to the global simulation's maximum resolution of 7.8 pc. I added a further six levels of refinement to reach a limited resolution of 0.1 pc. This is slightly larger than the idealised simulation case due to computational time. All gas denser than approximately $10\,\mathrm{cm}^{-3}$ was resolved to at least 512^3 (level 3).

3.2.1 Star Particle

Star particles form in the simulation when the gas flow converges into a (maximum refined) cell with a density greater than $10^4\,\mathrm{cm}^{-3}$ and a temperature $\leq 10\,\mathrm{K}$. This threshold is user-defined, and I selected it to be the value at which star formation is observed to occur inside a GMC (Lada C. J., Lombaridi M. & Alves J. F. 2010; Ginsburg et al. 2012; Kainulainen et al. 2014). Since this density is significantly below stellar densities, the resulting particle is treated as a star cluster. When a star particle is formed, half the mass is removed from the cell to create the initial particle. The star particle's velocity is the average of the neighbouring cells to prevent a runaway phenomenon. In addition, to avoid too many radiation sources in a small region, any new stars forming within 3 pc of an accreting star are merged. This mass accretion is from a sphere of cold ($T < 10^3\,\mathrm{K}$) gas whose size is defined at each time step in two ways in the calculations. The first method is the default scheme used within *Enzo*. A sphere is found such that its average gas density corresponds to a dynamical time, $t_{\mathrm{dyn}} = 0.5\,\mathrm{Myr}$; approximately one free-fall time for gas at the threshold density of $10^4\,\mathrm{cm}^{-3}$. The second method uses the Bondi-Hoyle accretion radius (or a gravitational capture radius), defined as $R_{\mathrm{BH}} = 2GM/(v^2 + c_s^2)$, where G is the gravitational constant, M is the star particle mass, v is the relative velocity between the star particle and the accretion sphere gas, and c_s is the sound speed. This radius indicates the region in which gas will be caught by the star's gravitational potential.

The typical accretion sphere size of the second Bondi-Hoyle method is smaller than the free-fall time sphere, leading to a lower accretion rate and smaller stars. For these simulations, the typical size of the free-fall time sphere is approximately $\sim 4 \times \Delta x_{\mathrm{min}}$, where the smallest cell size, $\Delta x_{\mathrm{min}} =$

0.05. We can estimate the Bondi-Hoyle accretion radius for a star particle of $1\,\mathrm{M}_\odot$ and $c_s = v = 0.3\,\mathrm{km\,s^{-1}}$ to give $R_{\mathrm{BH}} \sim 0.05\,\mathrm{pc}$. This corresponds to roughly one minimum cell size, Δx_{min}. For higher particle velocities, the accretion radius will shrink and be rounded back to one cell, whereas for larger star particles of $100\,\mathrm{M}_\odot$, the radius extends to $\sim 0.2\,\mathrm{pc} \sim 4\times\ \Delta x_{\mathrm{min}}$. As most have mass less than $100\,\mathrm{M}_\odot$, this gives a smaller typical accretion radius.

Due to these differences in accretion radii, I define this as the 'weak' accretion model as that where the Bondi-Hoyle accretion radius is used and the free-fall time sphere as the 'strong' accretion model. The accretion continues to increase the star's mass for one dynamical time or until the particle hits $800\,\mathrm{M}_\odot$. This star formation scheme is a slightly modified version of the cosmological star cluster method in Wise et al. (2012). Since I resolve down to the masses of individual stars (although not to stellar densities), the ionising luminosity is likely an overestimate. The radiative feedback should therefore be considered as an upper limit.

3.2.2 Supernova Feedback

In one simulation, I also include thermal feedback from supernovae explosions. After 4 Myr, massive clusters with $M > 100\,\mathrm{M}_\odot$ deposit thermal energy equal to $1 \times 10^{49}\,\mathrm{erg\,M_\odot^{-1}}$ into its surrounding cell. This is equivalent to one supernova per $100\,\mathrm{M}_\odot$ depositing $\sim 10^{51}\,\mathrm{erg}$ of energy; a frequency consistent with the Salpeter IMF for the cluster. Since supernova are actually distributed in time between 4–40 Myr, the deposit of energy at the lower limit of 4 Myr suggests this feedback rate is the upper limit (Krumholz et al. 2014). After 4 Myr, the star effectively 'dies' and stops radiating. In the simulations without supernovae feedback, star particles continue to radiate indefinitely.

3.3 Initial Conditions

I consider two separate initial conditions in this paper. The first uses an idealised Bonnor-Ebert profile for the cloud, while the second extracts a cloud that formed in a global galaxy simulation.

3.3.1 Bonnor-Ebert cloud

The idealised cloud takes the density profile of a Bonnor-Ebert sphere (Bonnor 1956); a hydrostatic isothermal self-gravitating sphere of gas that is con-

fined by its external pressure. The equation of equilibrium between pressure and self-gravity with a spherical symmetric is given by,

$$\frac{dp(r)}{dr} = -G\frac{M(<r)\rho(r)}{r^2}, \tag{3.1}$$

where r, $p(r)$, $M(<r)$ and $\rho(r)$ are a radius, thermal pressure at r, the enclosed mass inside r and gas density at r, respectively. The pressure of isothermal ideal gas is given by

$$p(r) = c_s^2\rho(r). \tag{3.2}$$

Then dimensionless equations are given by,

$$\xi = \frac{r}{c_s/\sqrt{4\pi G\rho_0}}, \tag{3.3}$$

$$\phi = -\ln\left(\frac{\rho}{\rho_0}\right), \tag{3.4}$$

$$\frac{1}{\xi^2}\frac{d}{d\xi}\left(\xi^2\frac{d\phi}{d\xi}\right) = e^{-\phi}, \tag{3.5}$$

where ρ_0 is the central cloud density, ξ is the dimensionless radius and ϕ is the dimensionless gravitational potential. The density distribution is given by the solving the equations numerically with $\phi|_{\xi=0} = 0$ and $d\phi/d\xi|_{\xi=0} = 0$.

While such a profile is derived analytically, there is observational evidence of their existence in nature, such as the Bok Globule B68 (Alves et al. 2001). The clouds slightly exceed the maximum stable mass for the Bonner-Ebert profile and therefore begin to collapse after the start of the simulation. The resulting cloud has a mass of $9.64 \times 10^4\,\mathrm{M}_\odot$, with an initial radius of 36.3 pc.

The cloud is given additional internal support from an initial injection of turbulence, produced by imposing a velocity field with power spectrum $v_k \propto k^{-4}$. This corresponds to the expected spectrum given by Larson for GMCs (Mac Low et al. 1998; Larson 1981). The turbulence slows the collapse as the gas cools and creates a filamentary structure of dense regions, instead of a centralised collapse. Since I did not want the cloud to be strongly distorted by its turbulence, I removed the lower order modes to avoid the large-scale perturbations. I also used an upper limit, corresponding to a maximum k-mode that was 1/10th of the number of cells across the cloud. This was to ensure adequate resolution of the included modes. This selection corresponded to $6 < k < 19$ for the GMC. The turbulence amplitude was set

Table 3.1: Idealised (Bonnor-Ebert) cloud parameters

$\Delta x_{\rm min}$	0.05	pc
$R_{\rm c}$	36.3	pc
$M_{\rm c}$	9.65×10^4	$M_\odot$
$T_{\rm c}$	1200	K
$\bar{\rho}_{\rm c}$	19.5	$\rm cm^{-3}$
$t_{\rm c,ff}$	12.0	Myr
$\sigma_{\rm c}$	3.77	$\rm km\ s^{-1}$

Table 3.2: Extracted cloud parameters

$\Delta x_{\rm start}$	7.8	pc
$\Delta x_{\rm min}$	0.12	pc
Main clump radius, $R_{\rm c}$	26.2	pc
Main clump mass, $M_{\rm c}$	4.4×10^6	$M_\odot$
$M_{\rm total}$	1.4×10^7	$M_\odot$

by the Mach number, $\mathcal{M} \equiv \sigma_{\rm c}/c_s$, where $\sigma_{\rm c}$ is the velocity dispersion inside the cloud and c_s is the sound speed. At the start of the simulation, the initial temperature is the Bonner-Ebert equilibrium temperature of 1200 K and $\mathcal{M} = 1$. The cloud cools rapidly, leaving the turbulence to support the cloud. A summary of the cloud properties is shown in Table 3.1.

This cloud was used in four simulations: (1) without feedback, (2) with the strong feedback from the free-fall time accretion radius, (3) with the weak feedback using the Bondi-Hoyle accretion radius and (4) with the addition of supernovae feedback. In all cases, the evolution time for the run was one free-fall time, corresponding to 12 Myr.

3.3.2 Extracted cloud

The second set of initial conditions extracts a cloud from a global galaxy disc simulation. The global simulation was also run using *Enzo* and is described in detail in Benincasa et al. (2013). The galaxy has the form of a Milky Way-type disc, with a flat rotation curve of $200\,\rm km\,s^{-1}$. A rotating frame of reference exists at a radius of 6 kpc, making gas at that radius stationary with respect to the grid, while gas at smaller and larger radii flows in opposite directions. This minimises the artificial support from the Cartesian mesh. The clouds are identified as connected cells with density over $100\,\rm cm^{-3}$ (details in Tasker & Tan (2009)) and their properties are found to agree well with those

Table 3.3: Simulations performed. Columns show run number, the initial conditions (idealised Bonnor-Ebert or extracted global simulation cloud), the method for calculating the accretion radius, inclusion of photoionising radiation, whether the star radiates continuously from formation (on) or stops after 4 Myr (off), inclusion of supernova and minimum cell size.

Run	IC	Accretion	Radiation	Cont.	SNe	$\Delta x_{\rm min}$(pc)
1	BE cloud	strong	off	n/a	off	0.05
2	BE cloud	weak	off	n/a	off	0.05
3	BE cloud	strong	on	on	off	0.05
4	BE cloud	weak	on	on	off	0.05
5	BE cloud	strong	on	off	on	0.05
6	BE cloud	strong	off	n/a	off	0.025
7	BE cloud	strong	on	on	off	0.025
8	Sim. Extract	strong	off	n/a	off	0.1
9	Sim. Extract	strong	on	on	off	0.1

observed in nearby disc galaxies. Clouds from this simulation were extracted to be used as initial conditions for more detailed star formation calculations and can be found online at `http://www.physics.mcmaster.ca/mcclouds/`. In this online catalogue, I used cloud with tag number 1149.

The extracted region is 500 pc across and contains a total gas mass of $1.4 \times 10^7\,{\rm M}_\odot$. Within the box, there is the central body of the cloud which has two clumps of high density gas, surrounded by a lower density network of tidal tails from these clumps interacting. The larger of the two clumps has a mass of $4.4 \times 10^6\,{\rm M}_\odot$ and radius of 26.2 pc while the smaller one is roughly half as massive, with $2.0 \times 10^6\,{\rm M}_\odot$ and 22.5 pc in radius. Unlike the idealised cloud case, this is clearly not a passive environment, but a fragmented and highly interactive location.

The Benincasa et al. (2013) simulation did not contain any star formation or feedback. While this had the advantage of resolving to higher resolutions more easily without having to negotiate large particle sizes, it did mean the gas had become very dense. Such a large pool of over dense gas would immediately turn to stars, producing an unphysical starburst and injection of feedback energy. To avoid this problem, I first evolved the gas for the crossing time of the box (calculated as the box size divided by the maximum velocity in the central clumps) equal to 6 Myr, and increased both the resolution and cooling to alter the minimum temperature from 300 K (used in the global model) to 10 K. I used a non-accreting star formation method,

which ate away at the dense gas, converting it into particles. After these 6 Myr, I then turned on the free-fall / strong accretion star formation model. Due to the heavy computation time, I performed this run with the strong accretion and without supernovae. The details of the simulation set-up are outlined in Table 3.2.

A summary of the performed runs in this paper is given in Table 3.3.

3.4 Results: Idealised Cloud

3.4.1 Cloud Morphology

The images in Figure 3.2 shows the gas surface density for simulations using the idealised Bonnor-Ebert sphere after one free-fall time (12 Myr) (Runs 1, 2, 3, and 4 in Table 3.3). The left panels show the simulation without any feedback, with stars formed using the strong accretion model (top) and the weak accretion model (bottom). The top-right panel include radiative feedback using the strong accretion model for the star formation while the bottom-right panel includes radiative feedback with the weak accretion model.

In all four cases, the initial turbulence in the gas causes it to form a filamentary and fragmented structure. As the gas cools, the turbulence decays and self-gravity dominates. The gas begins to collapse, increasing in density until the highest density regions reach the star-formation threshold. In the absence of any stellar feedback, the formation of stars does not halt the collapse, which continues under the cloud's own gravity. At the time shown for the non-feedback case, the gas is collapsing inwards with an average radial rate of -3.4 $\mathrm{km\,s^{-1}}$.

When radiative transfer is included in the simulation, the forming star particles generate thermal pressure that counters the collapse. With the weak accretion model, the gas is left expanding at an average radial rate of 1.7 $\mathrm{km\,s^{-1}}$. This increases to 3.5 $\mathrm{km\,s^{-1}}$ for the stronger accretion model, removing all dense gas from the central region. These results strongly suggest that star-forming clouds are heavily impacted by their stellar-feedback and can even be disrupted.

3.4.2 Star Distribution

Figure 3.3 shows the projected position of the star particles that formed in each cloud in Figure 3.2. The black dashed line marks the radius of the initial cloud. The particles are connected with lines that represent a

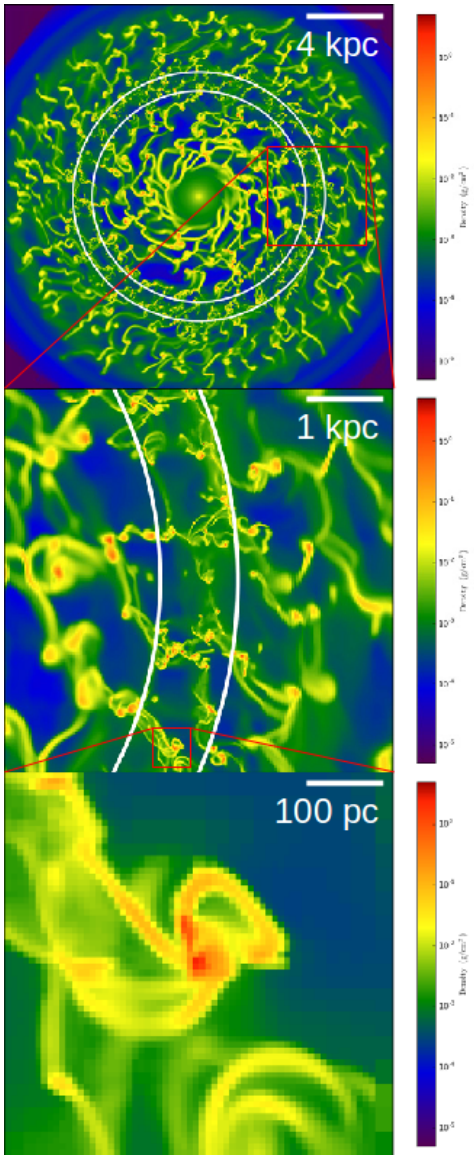

Figure 3.1: Three column density of a galactic disc simulation performed by Benincasa et al. (2013), the 20 kpc across full disc (top), zoomed-in 5 kpc across region (middle), and close-up of the extracted 500 pc across region used in this study (bottom). The white circle lines show the co-rotating frame.

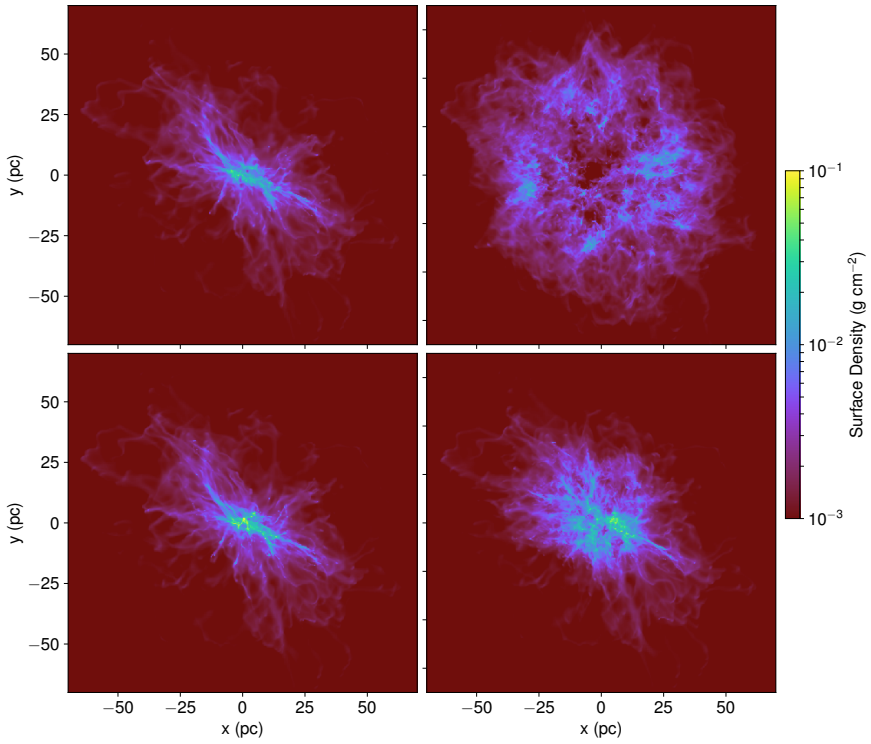

Figure 3.2: Comparison of the gas surface density for the idealised Bonnor-Ebert cloud when no feedback is included (left), feedback (right) using the strong accretion model (top row) and feedback using the weak accretion model (bottom row) after one free-fall time (12 Myr). The average outward radial velocity for the no feedback clouds is -3.4 (collapsing), and 3.5 and $1.7\,\mathrm{km\,s^{-1}}$ for the feedback using the strong accretion model and the weak accretion model, respectively.

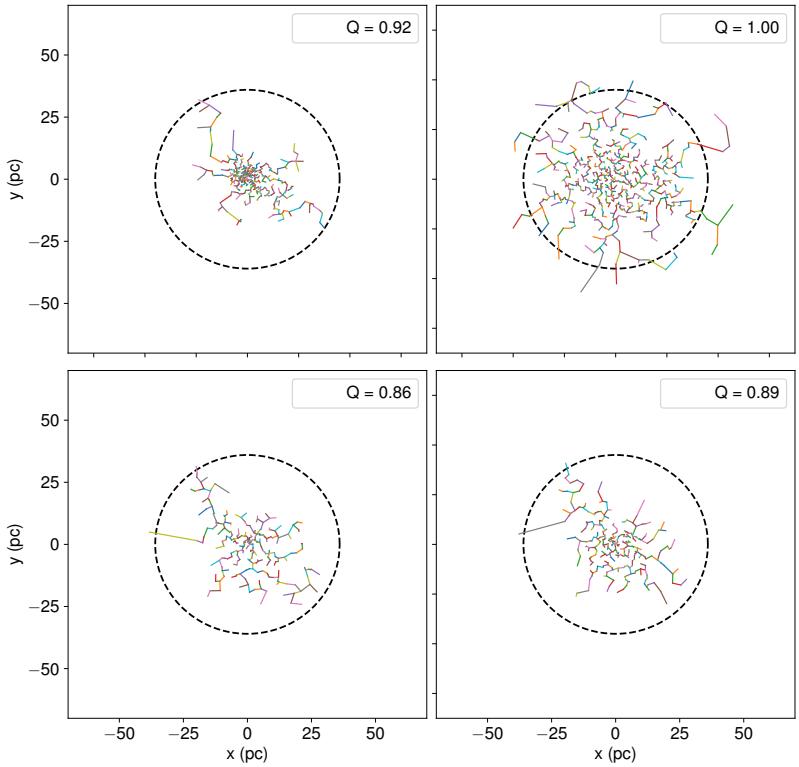

Figure 3.3: Comparison of the star particle distribution corresponding to each image in Figure 3.2. The solid lines show the minimum spanning tree (see section 3.4.2) which connects all the star particles. The quantitative description of the fragmentation, Q, is shown in the top right corner of each panel. The black dashed-line marks the initial cloud radius.

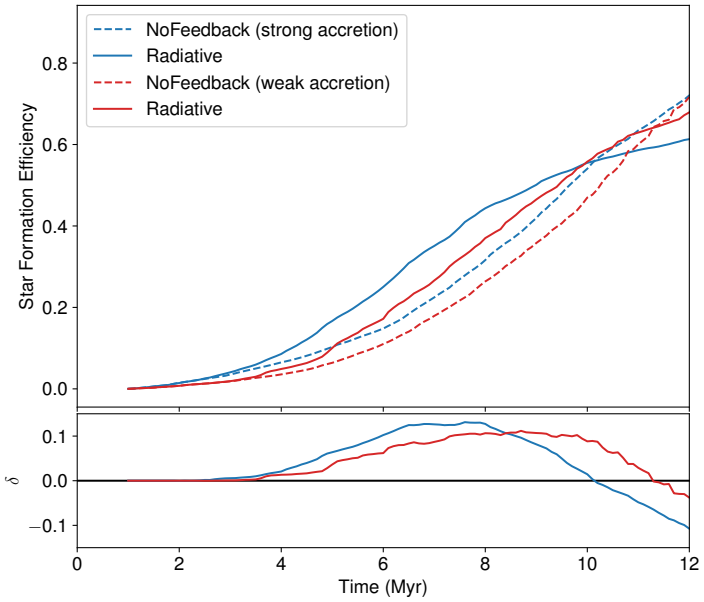

Figure 3.4: Comparison of the star-formation efficiency between runs with no feedback (dashed lines) and runs including radiative feedback (solid lines). Models that use the weak accretion model are in red, while the results from the strong accretion model are in blue. These are runs 1–4 in Table 3.3. The star formation efficiency is defined as $M_{\rm star}(t)/M_{\rm cloud}(t=0)$. Δ shows the difference between solid and dashed lines, with a +/- value indicating the positive/negative effect of feedback.

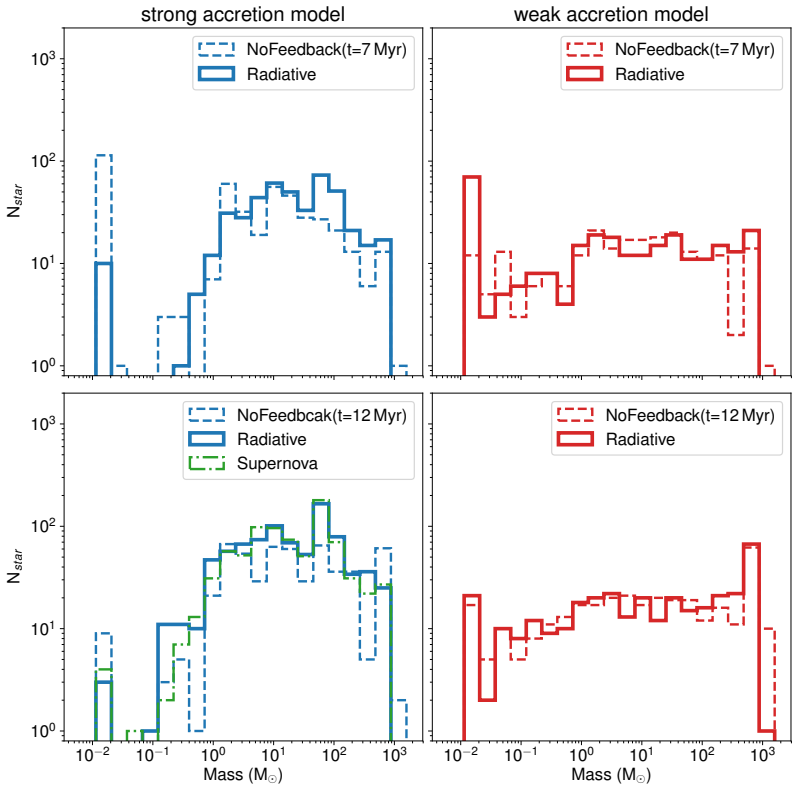

Figure 3.5: Comparison of the stellar mass distribution at 7.0 Myr (top row) when the effect of feedback is positive (boosting star formation) and at 12.0 Myr (bottom row) when it is negative. Dashed lines show simulations without feedback, while solid lines are for radiative photoionising feedback. (Runs 1 - 4 in Table 3.3.) Green dotted line shows the simulation that also includes supernovae feedback (Run 5). The left-hand panels in blue are for the strong accretion model, while the right-hand panels in red show results for the weak accretion model.

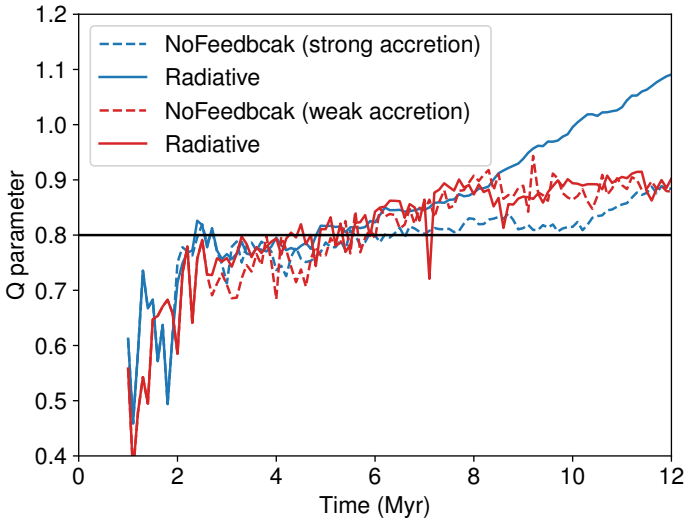

Figure 3.6: Comparison of the Q-parameter for each of the first four runs with the idealised cloud. A value of $Q \simeq 0.8$ indicates a constant volume density of stars through the cloud, while higher and lower values suggest a concentrated and more fractal distribution, respectively.

'minimum spanning tree' whereby all points are linked such that the total length of the connecting lines is minimised and there are no closed loops. Using this structure, a quantitative value (Q) was developed by Cartwright & Whitworth (2004) for defining how stars are distributed within a cluster or (in my case) cloud. This Q-parameter is defined as:

$$Q = \frac{\langle l \rangle}{\langle s \rangle} \tag{3.6}$$

where $\langle l \rangle$ is the mean length in the minimum spanning tree between star particles and $\langle s \rangle$ is the average separation between any two particles. If the stars are distributed evenly through the cloud to produce a uniform volume density, then $Q \simeq 0.8$. Values higher than this indicate that the stars are more centrally concentrated, while lower values imply a fragmented, fractal distribution of the stellar population.

In all three cases for the idealised cloud, the Q value is higher than the uniform case, showing that the star formation activity is largest in the cloud centre. This is unsurprising, since the gas in that region begins with the highest density, reaching the star formation threshold to produce the first population of stars prior to any feedback. In the case with no feedback, the stellar population remains localised in the centre of the collapsing cloud, with only a small number of stars forming along filamentary structures perpendicular to the direction of collapse. When feedback is included in the weak accretion model, the star population spreads outwards as the global collapse is reversed to allow dense gas to form further from the centre. With feedback using strong accretion model, stars form much further from the central region as the gas more rapidly expands. A small number of star particles are even found at radii beyond the original cloud edge. These stars actually formed within the cloud boundary, but escaped outwards. Comparing with the above panel showing the gas surface density, it can be seen that the central stars must be older, as there is now very little dense gas in that region. Despite this significantly more distributed population, the Q value remains high, showing that there is still a steady gradient in the star population density towards the centre of the cloud, rather than multiple individual sites of high star formation activity. The evolution of the Q value over the cloud lifetime will be considered in section 3.4.5.

3.4.3 Star Formation Efficiency

How effectively the cloud converts its gas into stars is measured by the star formation efficiency (SFE), defined as the total stellar mass divided by the

initial gas mass:

$$\epsilon(t) = \frac{M_{\rm star}(t)}{M_{\rm cloud}(t=0)} \tag{3.7}$$

This is shown in Figure 3.4 for times throughout the simulation. The SFE for the non-feedback simulations is shown by the dashed thin red lines for the weak accretion case and dashed thicker blue lines for the strong accretion case. For when radiative feedback is included, the line is solid with red and blue once again showing the weak and strong accretion cases, respectively. The difference between the feedback and non-feedback runs for each type of accretion is shown by the value Δ in the bottom panel of that plot, where Δ is simply:

$$\Delta(t) = \epsilon_{\rm Feedback}(t) - \epsilon_{\rm NoFeedback}(t) \tag{3.8}$$

giving a positive value when the feedback promotes star formation and a negative value when the star formation is suppressed.

At roughly 2 Myr, the first star formed in the simulation finishes its accretion and begins to emit ionising radiation during the feedback runs. Shortly after this, all four runs begin to deviate to launch into a different SFE history. The inclusion of feedback initially promotes the production of stars, raising the SFE above the non-feedback runs in both the weak and strong accretion models. This is reflected in the Δ value, which climbs during the first half of the simulation. The origin of this increased SFE from feedback could come from a number of sources. Star formation could be triggered in the edges of swept-up expanding shells of gas, producing a small but numerous population. Alternatively, the freshly heated gas could prevent fragmentation, forming a larger reservoir for newly formed stars to accrete to create more stellar mass than that from multiple smaller star particles. In the next section, I will see it is this second option that promotes the SFE. The stronger accretion model also forms larger stars, giving a higher SFE than the weaker accretion model for both the feedback and non-feedback runs.

Just after half-way through the simulation, the Δ value for the strong accretion case turns over and begins to drop. This is followed at around 10 Myr by the weak accretion case. The positive effect of feedback to boost star production drops until it becomes negative, and its presence suppresses the SFE compared to the non-feedback simulations. At this point, the solid lines dropping below the dashed in the upper SFE plot. This reversal in the effect of the feedback is due to the dispersal of the dense gas. As the cloud continues to expand, the gas that has not yet collapsed into stars is spread over a wider area. Without feedback, this lower density gas can

continue to collapse into a late stage of star formation, but with the outward force of feedback, it is permanently dispersed. The switch between positive and negative feedback occurs first in the stronger accretion model, since the gas is being dispersed more rapidly by the larger stars producing stronger radiation.

Despite suppression from the feedback, at the end of the simulation the SFE for the whole cloud is very high, varying between 60–70 %. This corresponds to a star formation rate per free-fall time of $\mathrm{SFR_{ff}} \sim 0.5$. By contrast, observations of GMCs suggest values of a few percent Krumholz & Tan (2007). Our higher numbers stem from the gravitational potential of the cloud overtaking the internal kinetic energy as the turbulence decays and is not sufficiently driven by the internal feedback. This suggests observed clouds may be only locally collapsing and globally supported by externally-driven turbulence or possibly magnetic fields Federrath (2015).

3.4.4 The Stellar Mass Distribution

The range of masses of the star particles formed in the idealised cloud simulations are shown in Figure 3.5. In all four panels, the dashed line shows the non-feedback runs, while the solid line is for feedback. Blue lines (left-hand plots) show the star particle masses when the strong accretion is used, while the red lines (right-hand plots) are for the weak accretion. The top two panels show the stellar mass distribution half-way through the simulation at 7.0 Myr, when the effect of radiative feedback is positive and boosts the star formation. The bottom two panels shown the result at the end of the simulation, 12 Myr, where the feedback now suppresses the star formation compared to the non-feedback runs.

At 7 Myr, the strong accretion model has a median star particle mass of $1.0\,\mathrm{M_\odot}$. The total number of star particles formed in all simulations is very similar at roughly 400 particles, but their masses vary. The mass profile is more peaked for the strong accretion model than when the weak accretion model is used, reflecting the ability to form larger star particles more easily during the accretion phase. For the strong accretion run, the effect of feedback is to reduce the number of small star particles and form instead, larger stars. This suggests the impact of feedback here is not primarily to trigger a population of star particles in the expanding shells of gas, but to suppress fragmentation. The outer layers around a newly forming star are thrown outwards by the radiative feedback and heated. The surrounding gas therefore increases and warms, stopping its fragmentation but making it available to be accreted by nearby star particles which gain in mass.

To confirm this situation, we measured the average accretion rate for the star particles with and without feedback. The accretion rate increased when feedback was used by roughly a factor of 2.0, confirming that the feedback impact is to provide more gas to build larger stars. This is different from the triggered star formation scenario, where feedback drives expanding shells of gas which fragment into new stars in a 'collect and collapse' scenario. There is no evidence in the simulation of collect and collapse star formation and I see no evidence of an elevated star formation around expanding shells. This is contrary to the smaller clouds explored by Walch et al. (2013), who find that a central star can trigger further star formation around an expanding shell. In my simulations, the turbulent gas produces a complex structure of filaments within which the star is born and this makes it hard to create a well defined shell wall.

In the weaker accretion case, the feedback also increased the number of the most massive stars ($> 100\,\mathrm{M}_\odot$) through the same mechanism. However, there is also a boost in the quantity of the smallest stars around $0.01\,\mathrm{M}_\odot$. It could be that triggered star formation is occurring in the weaker accretion case as the slower expansion of the cloud promotes the dense gas shells. This is hard to confirm visually and these small particles are merged with close-by larger neighbours, causing them to disappear by the later bottom-right panel. The number of small stars does decrease between the two time steps in all runs. This is due to accretion increasing the mass of the stars and a smaller number of new stars being born at later times.

By the end of the simulation, the stellar mass distribution (bottom panels) shows that feedback has created generally more massive stars for the strong accretion case. There is a population of very massive ($> 1000\,\mathrm{M}_\odot$) particles for the non-feedback run, which correspond to the final gravitational collapse of the cloud. This situation is mirrored to a smaller extend in the weak accretion run, with feedback producing a slight excess of star particles with $M > 100\,\mathrm{M}_\odot$.

3.4.5 Q-parameter

The distribution of star particles through the cloud is shown by the evolution of the Q-parameter in Figure 3.6. In all runs, Q increases over time, indicating that a concentrated profile develops, with the largest number of star particles in the cloud centre. While the strong accretion feedback produces the highest number of star particles away from the core, as shown in Figure 3.2, it has the steepest gradient through the cloud, landing it a high Q value. Without feedback, most of the stars are in a smaller region around

the centre, producing a nearly uniform volume density with Q value slightly over 0.8. The weak accretion model is insufficient to change this significantly. These values are similar to those found from observations of GMCs, which display a range of Q-parameters from 0.7–1 in different clusters Sánchez & Alfaro (2010).

3.4.6 Supernovae Feedback

I performed one additional simulation using the strong accretion model with radiative feedback, where a massive star's radiation stops after 4 Myr, concluding with a supernovae thermal energy injection, as described in section 3.2.2. The difference the addition supernovae feedback makes is very small, since relatively few massive stars were formed in the simulation and the ionising radiation has already cleared away most of the gas. This can be seen in the lower right-panel of Figure 3.5. The stellar mass distribution is only weakly affected by the supernovae. At the lower mass end of the final stars formed ($< 1\,\mathrm{M}_\odot$), the supernovae run forms less stars than when the radiation continues steadily but slightly more of the smallest population of stars at $0.01\,\mathrm{M}_\odot$. This implies that a sudden thermal injection is less effective at changing the fragmentation and accretion rate than continuous radiation energy.

3.5 Results: Globally Simulated Cloud

I now change from looking at the effect of feedback on the idealised Bonnor-Ebert cloud structure, to that of a cloud formed in a global galaxy simulation, as described in section 3.3.2, and listed as runs 8 and 9 in Table 3.3.

This is a significantly different initial condition for the cloud. Formed in a dynamic environment feeling the effects of sheer and the gravitational pull of nearby clouds, the cloud here is not in equilibrium. Rather, it has already fragmented to produce a varied density structure. Below, I examine the impact of photoionisation on the cloud's late evolution.

3.5.1 Cloud Morphology

The morphology of the cloud after one crossing time (at 12 Myr) is shown in Figure 3.7. The panels show disc face-on projections of the gas surface density (top row) and the star particle positions and their minimum spanning tree (bottom). The left-hand side is for the run with star formation but no

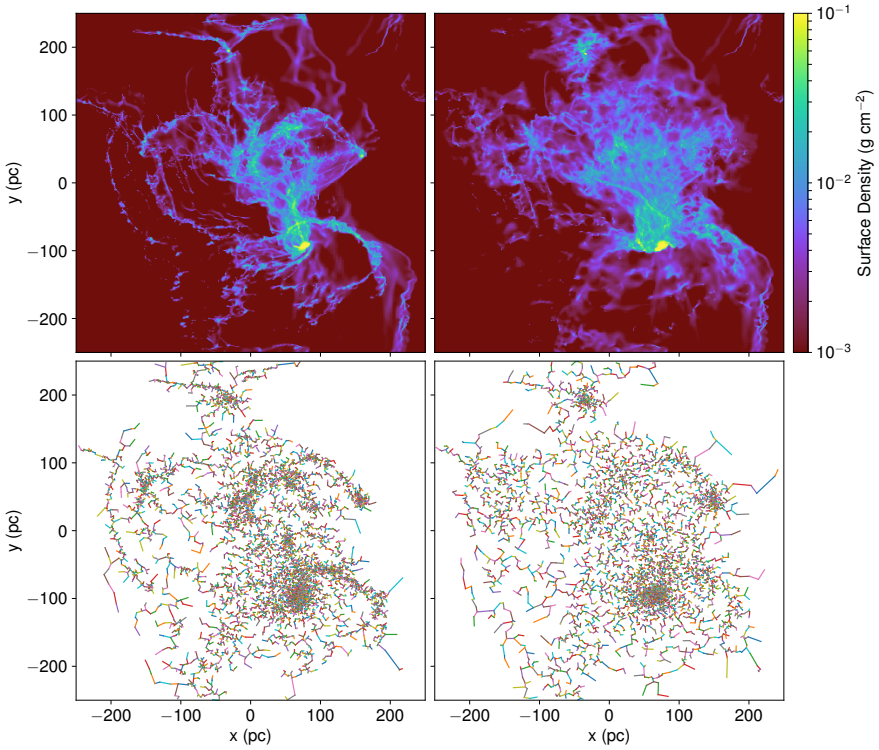

Figure 3.7: Comparison of the face-on gas surface density (top row) and the star particle distribution for the cloud extracted from the global model at 12 Myr. The lines in the bottom panels show the minimum spanning tree (see section 3.4.2). Left panels show the simulation without stellar feedback, while the right-panel includes radiative feedback.

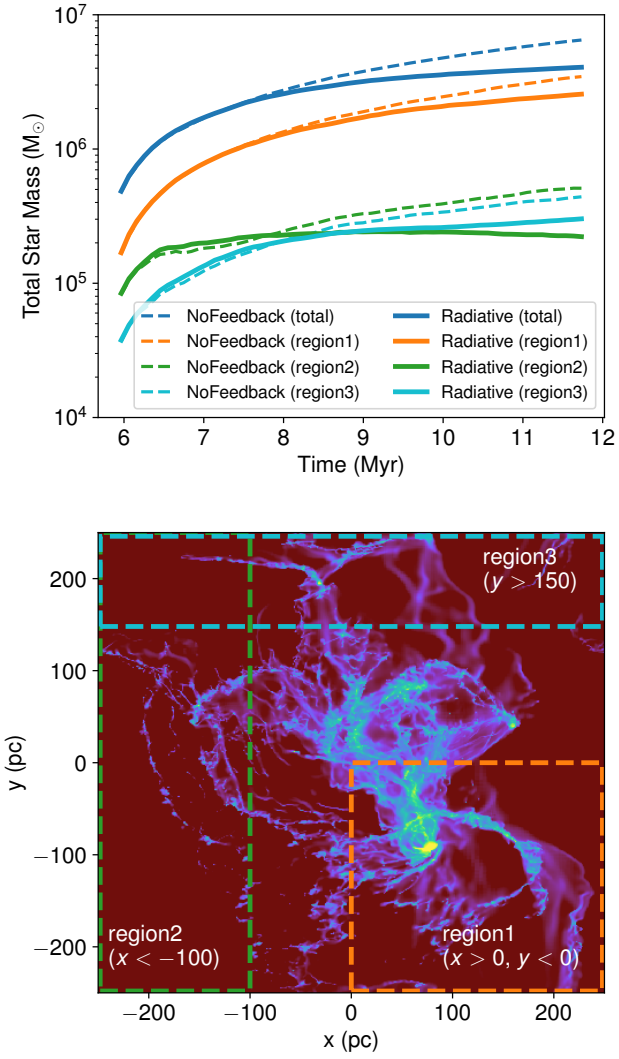

Figure 3.8: The evolution of the total star mass in the radiative feedback (solid lines) and non-feedback (dashed) simulations for different regions within the globally simulated cloud. Line colour corresponds to coloured box region, with the green region 1 containing the most high density gas, while regions 2 and 3 (red and blue) contain less dense material. The dark blue lines show the result for the whole box.

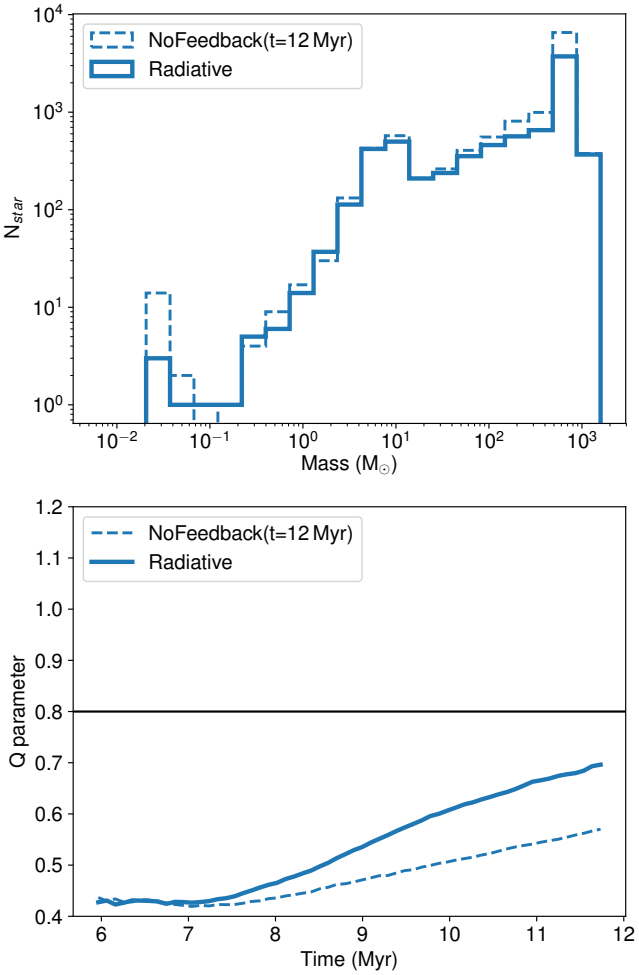

Figure 3.9: The stellar mass distribution at 12 Myr and Q-parameter for the globally simulated cloud for both non-feedback (dashed) and feedback runs for one crossing time after the star formation begins.

stellar feedback, while the right-hand images shown the effect of including photoionisation.

An immediate difference between this cloud and the idealised cases in the previous section is that the radiative feedback is making a much smaller impact on the cloud morphology. There is no evidence that the cloud is globally disrupted by the feedback. Rather, the changes appear on more local scales. The central dense region survives the injection of ionising radiation, but increases in radius. Surrounding pockets of dense gas also appear more diffuse and in the lower density filaments at the box edge, the feedback has disrupted their structure.

This is shown quantitatively by the star particle distribution and the Q-parameter in the lower panels. Without feedback, the stellar structure gives $Q = 0.6$, pointing to a fractal clustering of stars, rather than a uniform distribution or dominant centre. This agrees with the multiple small sites of dense (red) gas in the gas surface density above. Adding feedback increases Q to 0.72, implying that these centres have been partially disrupted to produce a more uniform distribution of stars.

3.5.2 Total Stellar Mass

Due to the simulated cloud containing a wide variety of environments, it is more helpful to look at the impact of feedback on different regions. Figure 3.8 shows the time evolution of the total stellar mass for both the non-feedback and feedback runs in the whole simulation box (dark blue) and in three different sub-regions. The regions are marked on the surface density image in the right-hand panel of the same figure. Region 1 (green lines) contains the densest clump in the box with an average gas density of $400\,\mathrm{cm}^{-3}$. Region 2 (red) and Region 3 (cyan) contain more low density gas, with the average in Region 2 of $230\,\mathrm{cm}^{-3}$ and in Region 3, $270\,\mathrm{cm}^{-3}$. Region 2 is very fractal, with a small Q (~ 0.4) and plenty of filamentary structure. Region 3 has a number of smaller star-forming clumps and a less fractal Q value at 0.6. As it is no longer clear in the simulated cloud exactly where the cloud edge is, the SFE is a less helpful quantity so I instead focused on the total star mass. The time evolution begins with the formation of the first radiating star particle, where the accretion radius corresponds to the strong radiative feedback mode.

In the densest Region 1, the addition of feedback has no effect on the star production for the first two million years. After that time, the two runs begin to deviate, with the feedback suppressing the star formation in the clumps. For the lower density Regions 2 and 3, the effect differs. Like the

idealised cloud, the initial impact of feedback is to promote star formation, causing the radiative simulation to have a slightly higher stellar mass over the first 3–4 Myrs. After that time, the feedback acts to suppress the star formation, making a larger difference to the gas than in the higher density Region 1.

This difference underscores the importance of the initial state of the gas. Radiative feedback in the simulations can only promote star formation if the gas is less dense. Within collapsing cores, its action is to lower the rate of star formation by providing a pressure to counterbalance the collapse. The pressure in this situation is not enough to overwhelm the self-gravity, but it can slow the production of star-forming gas.

Considering the gas in the entire box, the SFE reaches ∼50% when feedback is not includes and decreases to ∼30% with feedback, agreeing with the result that star formation is overall suppressed in this denser environment.

3.5.3 Stellar Mass Distribution and Q-parameter

The distribution of stellar masses in the globally simulated cloud is shown in the top panel of Figure 3.9, with the derived Q-parameter in the lower panel. Due to the larger amount of material available, gas in the simulated cloud collapses to form very massive stars. The density in these regions is too great to be disrupted by the feedback, which acts to slightly suppress the formation of stars with $M > 1\,\mathrm{M}_\odot$. Where smaller stars are forming, the feedback has a stronger effect, causing fewer stars with $M < 0.1\,\mathrm{M}_\odot$ to form. These lower mass stars are likely to be forming in lower density regions such as Region 2 and 3 in Figure 3.8, where the gas is much less fragmented and feedback can have a significant effect in diffusing the dense clumps.

The Q-parameter for the cloud's stellar population steadily rises over the course of the simulation. This suggests that the star formation is initially very fractal, forming in multiple pockets of over-dense gas. With feedback unable to break up the dense cores, the gas steadily collapses, moving towards a more uniform distribution of stars. Feedback promotes this process. By suppressing star formation in the densest regions, it allows the star particle distribution to even out as lower density gas begins to collapse.

Observations indicate that the Q-parameter tends to be higher than ~ 0.7, suggesting that this breaking of fractal structure by feedback is occurring in GMCs. Simulations performed by Dale et al. (2012b) indicate that this process is dependent on the gas density. In higher density regions, the feedback acted to raise Q, whereas in lower density gas it had the reverse

effect. Dale et al. (2012b) accounted for this difference by the denser gas more successfully forming 'collect and collapse' shells of star formation. My simulations do not show strong evidence of this mechanism, but the reduction of star formation in the dense cores still leads to more distributed star formation and a higher Q.

3.6 Discussion

3.6.1 Feedback: Positive or Negative?

The impact of radiative feedback differed strongly between the two cloud types: the idealised Bonner-Ebert sphere and the cloud extracted from the global simulation. The main difference between these two models was density. The idealised cloud initially had a smooth density profile, with an average value three orders of magnitude below the star formation threshold (see Table 3.1). The extracted cloud meanwhile, had evolved without forming stars in its global environment. It therefore has multiple regions that have already collapse to high density before the feedback was allowed to act. The difference produced the change between positive and negative feedback effects.

Both the weak and strong accretion models with feedback were effective in low density gas. As stars began to form, the feedback ejected the outer layers of gas and heated them, preventing further fragmentation and allowing neighbouring star-forming regions to accrete more effectively. The result was to increase the mass of the newly formed stars, creating a positive feedback effect on the total star formation. This continued until the star-forming regions became very dense. The feedback was then no longer able to eject hot gas into the regions surrounding the new star and could only slow the collapse of the dense gas. This reduced the star formation rate, producing a negative effect on star production.

In the extracted cloud, much of the gas was already at this later collapsed phase. The feedback there could only slow the collapse and reduce the star formation, but it could not disperse gas to increase accretion on neighbouring stars. This meant that the overall effect of the feedback was negative, suppressing the star formation. The only exception to this was in the low density regions of the simulation box, where a small positive effect could be seen on the gas that was newly collapsing.

This result agrees with findings by Dale et al. (2012), who noted that very massive clouds are largely unaffected by feedback due to their high escape velocities preventing gas escaping. We note the same effect on a small scale,

with feedback in star-forming clumps producing a negative effect due to the feedback being unable to escape and affect the surrounding medium.

3.6.2 The Effect of Resolution

I performed two extra simulations at a higher resolution with $\Delta x = 0.025\,\mathrm{pc}$, for idealised cloud using the strong accretion model, with and without radiative feedback. The trends observed, including the initial positive effect of the feedback changing to a negative impact, were unchanged. Figure 3.10 shows the evolution of SFE for these runs and the stellar mass distribution at the end of the simulation, which is a close match to Figure 3.4 and the left-bottom panel of Figure 3.5. This result therefore seems to be robust to resolution effects.

3.6.3 The Effect of Dust

One effect that I did not include in the calculations is that of dust. Dust grains can absorb photons in addition to the gas, potentially resulting in a smaller expansion of feedback-driven bubbles from radiation pressure. About 25% of the total photons may be absorbed by the dust assuming a Milky Way dust-to-gas ratio and then later re-emitted at infrared wavelengths McKee & Williams (1997). The impact of this process is difficult to estimate. Previous research suggests that the expansion of H II regions are primarily governed by thermal pressure except in dense starburst environments Krumholz & Matzner (2009). It is likely true that if the dust density follows that of the gas, the impact will remain strongly dependent on the cloud structure. A more detailed model is required to investigate this further.

3.7 Conclusions

I investigated the effect of photoionisation on two different cloud structures: an idealised Bonnor-Ebert sphere that was initially stable and a complex cloud structure extracted from a global galaxy simulation. The results are as follows:

1. photoionisation can both promote star formation (positive feedback) and suppress it (negative feedback). Which occurs depends on the density of the gas. High density regions that are undergoing gravitational collapse could not be dispersed by feedback. Instead, the

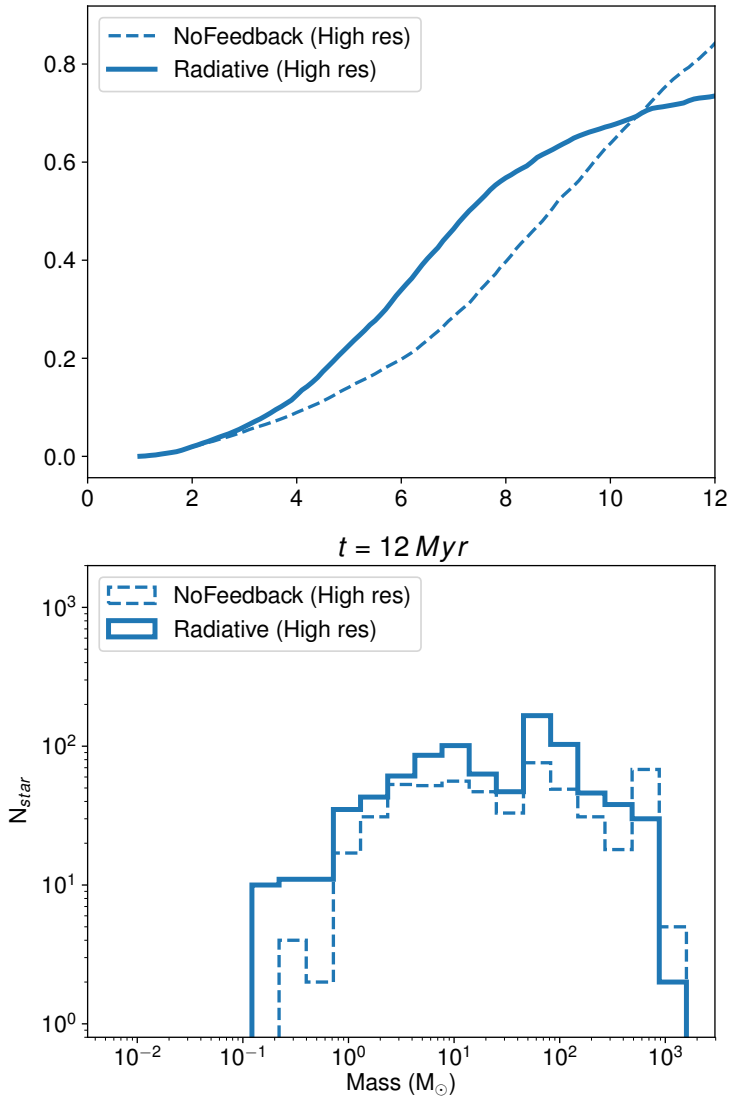

Figure 3.10: The SFE evolution (top) and the stellar mass distribution at 12.0 Myr for the idealised cloud at a factor of two higher resolution. The dashed line shows the simulation without feedback and the solid line is when radiative feedback is included. Δ in the top figure is the difference between the two runs, with a +/- value indicating a positive/negative effect from the feedback. Comparison with the main run in Figure 3.4 and Figure 3.5 shows that results are robust to resolution effects.

collapse was slowed to reduce the star formation rate. On the other hand, lower density regions could have their outer layers blown out by the radiative feedback. In this case, the surrounding medium increases in density and temperature to become a pool for accretion material. Nearby star-forming regions increased in mass to form larger stars.

2. The Q-parameter is a quantitative way of measuring the distribution of stars. Simple profiles like my idealised cloud move towards centrally concentrated profiles, even in the presence of feedback. The cloud formed in a global simulation had a more complex density structure, forming initially a more fractal distribution of stars that moved towards uniform as the gas collapsed.

3. My simulation did not show obvious triggering in expanding shells from the feedback. However, the complex structure of filaments within the cloud makes this hard to detect. Instead, I find feedback primarily increased the number of more massive stars formed due to bolstering the accretion rate.

4. The addition of a thermal feedback supernovae term did not made a significant difference to the star formation. The supernovae exploded late in the star's lifetime after the ionising radiation had removed any surrounding dense gas.

5. I tried two different models for star formation accretion, using different accretion radii. While the results were broadly the same, feedback was significantly more effective when the average star mass was larger. While not surprising, this emphasises the sensitivity of the results to the forming stellar population.

The ultimate conclusion is that the effect of feedback strongly depends on the gas structure. It is most effective when the gas is newly collapsing and has a far smaller impact on dense regions.

Chapter 4

From cloud crash to star birth

4.1 Abstract

I investigate star formation occurring in idealised giant molecular clouds, comparing structures that evolve in isolation versus those undergoing a collision. Two different collision speeds are investigated and the impact of photoionising radiation from the stars is determined. I find that a colliding system leads to more massive star formation both with and without the addition of feedback, raising overall star formation efficiencies (SFE) by a factor of 10 and steepening the high-mass end of the stellar mass function. This rise in SFE is due to increased turbulent compression during the cloud collision. While feedback can both promote and hinder star formation in the isolated system, it increases the SFE by approximately 1.5 times in the colliding case when the thermal speed of the resulting H II regions matches the shock propagation speed in the collision.

4.2 Numerical Methods

4.2.1 Sink Particle

Due to computational cost, there is a limitation of refining meshes. If gas continues to collapse at the finest level of refinement, the object can be no longer resolved. So, a sub-grid model is needed. Sink particles are introduced to convert gravitationally bound and collapsing gas into pressure-less particles. For each cell, a sink particle is formed when the following criteria

proposed by Federrath et al. (2010) are met: (a) A cell of species (j) is on the finest level of refinement. (b) The cell density (ρ_j) is greater than a threshold value ($\rho_{\rm th}$);

$$\rho_j > \rho_{\rm th}, \tag{4.1}$$

where $\rho_{\rm th}$ is given by

$$\rho_{\rm th} = \pi \frac{c_s^2}{G\lambda_{\rm J}^2} = \pi \frac{c_s^2}{G(\Delta x_{\rm min})^2}. \tag{4.2}$$

The $\Delta x_{\rm min}$ is the minimum cell size and $\lambda_{\rm J}$ shows the minimum Jeans length we can resolve with five cells at the maximum refinement level. (c) The gas within a accretion sphere is not within other accretion spheres, in other words, the all distance from the existing sinks must be larger than twice the accretion radius,

$$|\boldsymbol{x}_j - \boldsymbol{r}_i| > 2r_{\rm acc} \text{ for all } i, \tag{4.3}$$

where $\boldsymbol{x}_j$ is the cell position, $\boldsymbol{r}_i$ is the existing sink positions and $r_{\rm acc}$ is the accretion radius. The accretion radius has $2.5\Delta x_{min}$ in this study. (d) Gas is converging towards the center,

$$\frac{(\boldsymbol{v}_i - \boldsymbol{v}_j)\cdot(\boldsymbol{x}_i - \boldsymbol{x}_j)}{|\boldsymbol{x}_i - \boldsymbol{x}_j|} < 0 \text{ for } i\text{: } |\boldsymbol{x}_i - \boldsymbol{x}_j| < \sqrt{3}\Delta x_{min}, \tag{4.4}$$

where $\boldsymbol{v}$ is the cell velocity. We must remember that this is cell-centered velocity and different with the *Zeus* formalism. (e) The gravitational potential is minimum within the accretion sphere,

$$\phi_j < \phi_i \text{ for } i\text{: } |\boldsymbol{x}_i - \boldsymbol{x}_j| \leq r_{\rm acc}, \tag{4.5}$$

where ϕ is the gravitational potential. (f) Gas within the accretion sphere is Jeans unstable for collapse,

$$|E_{\rm grav}| > 2E_{\rm th}, \tag{4.6}$$

where $E_{\rm grav}$ and $E_{\rm th}$ are the total gravitational energy and total thermal energy within the accretion sphere, respectively. Finally, (g) gas within the accretion radius is gravitationally bound,

$$E_{\rm grav} + E_{\rm th} + E_{\rm kin} < 0, \tag{4.7}$$

where $E_{\rm kin}$ is the total kinetic energy within the accretion sphere. Those total energies are calculated as follows,

$$E_{\rm grav} = \sum_i m_i \phi_i, \tag{4.8}$$

$$E_{\rm th} = \sum_i m_i e_i, \tag{4.9}$$

$$E_{\rm kin} = \sum_i \frac{1}{2} m_i |\boldsymbol{v}_i - \boldsymbol{v}_j|^2, \tag{4.10}$$

where m is the cell mass. Any magnetic fields support does not included in this study.

When a sink is formed, gas over the threshold density is removed from the cell to create the initial particle's mass. The sink is given the average velocity of the neighbouring cells, avoiding the potential for a runaway particle. The sink can also accrete gas over the threshold density within the accretion sphere if the gas is bound to that sink. The accretion continues for one local dynamical time (the free-fall time inside the accretion sphere) or until the sink mass hits $50\,{\rm M}_\odot$; a cluster mass that is liable to contain at least one massive star based on a Salpeter IMF between 1–$100\,{\rm M}_\odot$. If another particle enters the accretion sphere during the accretion phase, the sink particles will merge if they are bound. The calculation of gravity from sinks is coupled with hydrodynamics by using the second-order cloud-in-cell (CIC) interpolation technique.

4.3 Initial Conditions

I consider three sets of initial conditions. The first simulation is an isolated cloud, while the second and third sets are small and large clouds with differing collision velocities. A summary of the cloud properties is shown in Table 4.1. The simulation box size is 120 pc along each side, covered by a root grid with 128^3 cells, with two additional static meshes that are located at the position of the clouds throughout the simulation. An additional three levels of adaptive refinement are used, based the Jeans length requirement. At the maximum refinement level, the cell size is 0.029 pc. At the maximum refined meshes, I uses an accretion radius of 0.073 pc and a threshold density of $\rho_{\rm th} = 7.0 \times 10^{-20}\,{\rm g\,cm^{-3}}$, which is above the observed value ($10^4\,{\rm cm^{-3}} \simeq 3 \times 10^{-20}\,{\rm g\,cm^{-3}}$) for star formation to occur (Lada C. J., Lombaridi M. & Alves J. F. 2010; Ginsburg et al. 2012; Kainulainen et al. 2014).

	isolated	small	large	
r_c	24.5	11	22	pc
M_c	5.5	1.1	4.4	$\times 10^4\,M_\odot$
T_c	580	260	520	K
$\bar{\rho}$	6.1	13.6	6.8	$\times 10^{-23}\,g\,cm^{-3}$
t_{ff}	8.5	5.7	8.0	Myr
σ_c	3.8	2.7	3.5	$km\,s^{-1}$

Table 4.1: Idealized (Bonnor-Ebert) cloud initial parameters: radius, mass, temperature, average density, free-fall time and velocity dispersion.

4.3.1 Isolated Cloud

The isolated cloud takes the density profile of a Bonner-Ebert sphere (see section 3.3.1). The sphere is unstable if its dimensionless radius exceeds a critical value of $\xi_{crit} = 6.45$. In this study, spheres sit at the slightly higher value of $\xi = 7$ and therefore begin to collapse after the start of the simulation. The mass of the isolated cloud is equal to the combined mass of the two colliding clouds. The clouds are surrounded by low density (1.4×10^{-24} g cm^{-3}) background gas at 10^4 K.

The cooling of the gas is initially compensated by an initial injection of turbulence that imposes a velocity field within the cloud. This is described in detail in Takahira et al. (2014). In brief, a velocity power spectrum of $v_k \propto k^{-4}$ is added to the gas, corresponding to the expected spectrum given by Larson for GMCs (Larson 1981; Mac Low et al. 1998) and appropriate for the supersonic turbulence seen in molecular clouds (Federrath 2013). This creates a filamentary density structure (Arzoumanian et al. 2011; Federrath 2016), rather than a centralised collapse. The initial amplitude of the turbulence is dictated by the sonic Mach number. Initially the cloud has a high equilibrium temperature and then the Mach number is 1.0, but the cloud cools within a few Myrs, which is shorter than the crossing time (~ 10 Myr). After this, the turbulence is supersonic with a typical Mach number of 10.

4.3.2 Colliding Clouds

For the simulations of colliding clouds, I evolve the clouds in a stationary position for 0.5 Myr to allow the development of the turbulent density structure. The smaller cloud is then given a bulk velocity of 10 $km\,s^{-1}$ or 20 $km\,s^{-1}$ in the direction of the larger cloud to form a head-on collision. These velocities were based on simulations performed by Takahira et al.

(2014), who found that slower velocities did not result in a strong shock front while a faster collision completed the interaction before the dense gas had time to collapse. This sweet spot of around $10 - 20\,\mathrm{km\,s^{-1}}$ also appears to be supported by the observed collision velocities of clouds around super star clusters.

4.4 Results & Discussions

To assess the impact of both the collision and feedback, this section will first look at the comparison of the isolated and colliding clouds where sink particles do not emit ionising radiation. The final part of this section will consider the addition of this feedback.

4.4.1 Gas Structure

Figure 4.1 shows the surface density along the z-axis at 0.5 Myr when the turbulent structure has been established (top panels) and at 4 Myr (bottom panels) which is a main analysis time. The left-hand panels show the isolated cloud, while the right-hand panels show the colliding clouds with velocity $10\,\mathrm{km\,s^{-1}}$. The analysis time for comparing the isolated and colliding clouds was chosen to be half the free-fall time of the isolated (and largest colliding) cloud. The range of densities within the cloud gas can be seen in the one-dimensional density probability distribution functions (PDF) in Figure 4.2, for the analysis time of 4 Myr. The blue dotted line shows the isolated cloud, while the orange dashed and green dot-dashed lines are for the clouds that collided with $10\,\mathrm{km\,s^{-1}}$ and $20\,\mathrm{km\,s^{-1}}$, respectively. The black vertical line shows the density threshold for the sink particle creation. Gas to the right of this line is therefore eligible to be converted into stars, assuming it is gravitationally bound to a sink.

At the sink threshold, the colliding cloud systems both have over a factor of ten more dense gas than in the isolated case. This extends into a power-law tail that is expected when gravity starts to dominate over turbulence (Klessen 2000; Kritsuk et al. 2011; Federrath & Klessen 2013; Schneider et al. 2013; Kainulainen et al. 2014). The excess dense gas is from the interface of the collision which creates a bow-shaped shock as the smaller cloud penetrates the body of the larger GMC (see Takahira et al. (2014) for images of the evolution of the collision). The result is a substantially broader PDF profile, demonstrating that compressive turbulence is being driven by the collision of the clouds (Federrath et al. 2008; 2010). This is expected to lead to an enhanced star formation rate (Federrath & Klessen 2012). Notably, gas

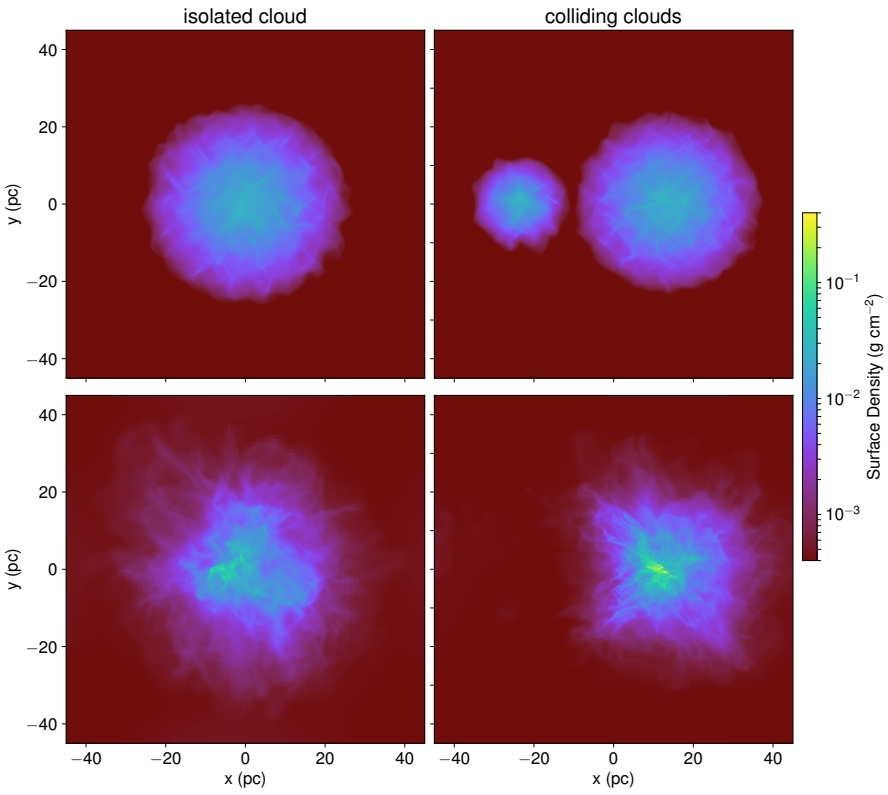

Figure 4.1: (Top) Surface density of the isolated (left) and colliding clouds (right) after 0.5 Myr and (bottom) at the main comparison time after 4 Myr. Shown is the colliding case without feedback for a collision velocity of $10\,\mathrm{km\,s^{-1}}$.

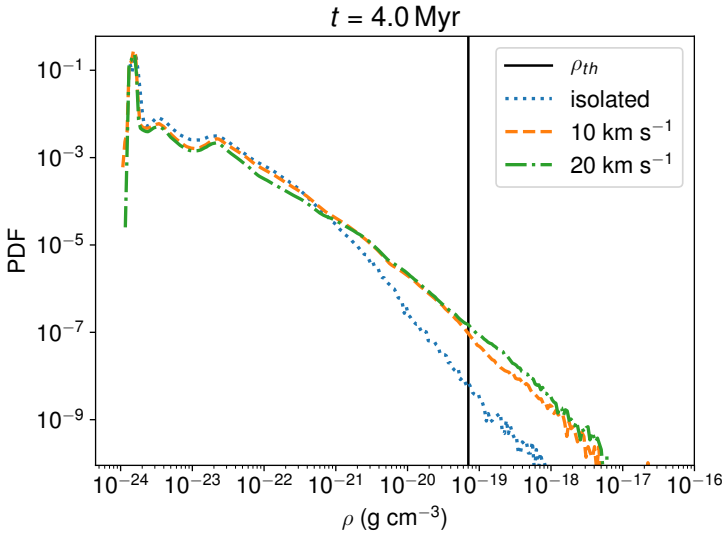

Figure 4.2: The probability distribution function for the isolated (blue-dot) and two colliding cloud systems (orange-dash and green-dot-dash) at 4 Myr. The clouds involved in the collision have wider PDFs due to the rise in compressive turbulence.

with densities higher than the sink formation threshold is not being instantly converted into sink particles because of the sink creation criteria of bond and collapsing gas introduced by Federrath et al. (2010) (see method section). This suggests that while dense, the turbulence is kinetically supporting the gas against collapse and preventing it being immediately available for sink creation. Larger cores with masses able to dominate the turbulence should therefore be favoured and will accrete from the surrounding gas to form the massive clusters seen in observations of cloud collisional systems (Fukui et al. 2016). This will be shown explicitly below. Between the two collision velocities, the gas distributions are similar, with the faster impact producing slightly more dense gas beyond the sink threshold.

4.4.2 Star Formation

How actively the cloud converts its gas into stars can be measured by looking at the cloud's star formation efficiency (SFE), defined as $\epsilon(t) = M_{\rm star}(t)/M_{\rm cloud}(t = 0)$, where $M_{\rm star}$ is the total mass in stars at time t, and $M_{\rm cloud}$ is the total cloud mass (for the colliding case, for both clouds) at the start of the simulation. The evolution of the SFE is plotted in Figure 4.3 for the isolated (blue-dot) and two colliding systems (orange-dash and green-dot-dash) without photoionising feedback.

Initially, the gas is not dense enough to form sink particles. Thermal support decreases as the gas cools, then stars start to form earlier than the global collapse timescale (t_{ff} ~8 Myr) due to local compression by turbulence. The first star forms in the isolated cloud at 2.7 Myr, but very few stars are formed until after 5 Myr where the cloud's gravity finally overwhelms the decaying turbulence and begins to collapse. This leads to the global collapse of the isolated cloud. Without a fresh form of support from stellar feedback, the number of stars in the isolated cloud increases rapidly, reaching an efficiency of about 2% by 6 Myr.

The colliding clouds begin star formation earlier, starting at 2.0 Myr and 2.2 Myr for the 10 km s^{-1} and 20 km s^{-1} collision velocities respectively. The clouds begin their collision at 1 Myr for the 10 km s^{-1} and 0.8 Myr for the 20 km s^{-1} cases, so star formation begins about 1 Myr after the shocked interface begins to form. Sink particles form rapidly in the dense shock front, producing a significantly higher star formation rate (the gradient of the SFE curve) than for the isolated case. The collision at 20 km s^{-1} produces a denser shock front than the slower collision, increasing the stellar production rate still further. At 4 Myr, the 10 km s^{-1} collision case is forming stars 18 times faster than for the isolated cloud, while the 20 km s^{-1} collision case is

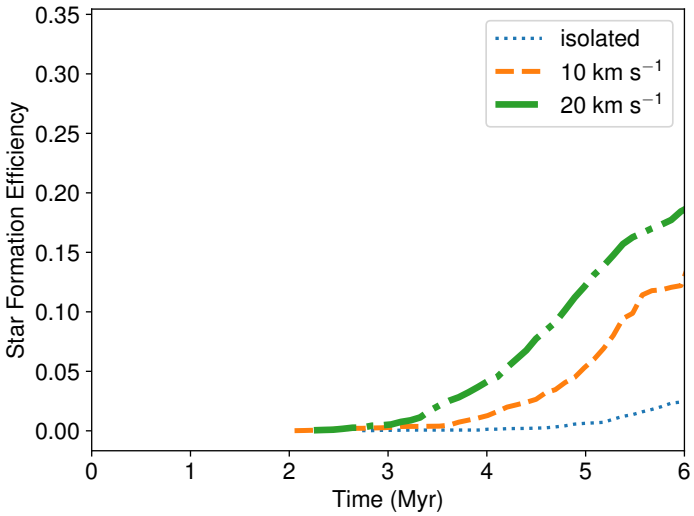

Figure 4.3: The star formation efficiency for the simulations without feedback. The blue dotted line shows the isolated cloud case, the orange dashed line is for the clouds colliding at $10\,\mathrm{km\,s^{-1}}$ and the green dot-dashed line is for the faster $20\,\mathrm{km\,s^{-1}}$.

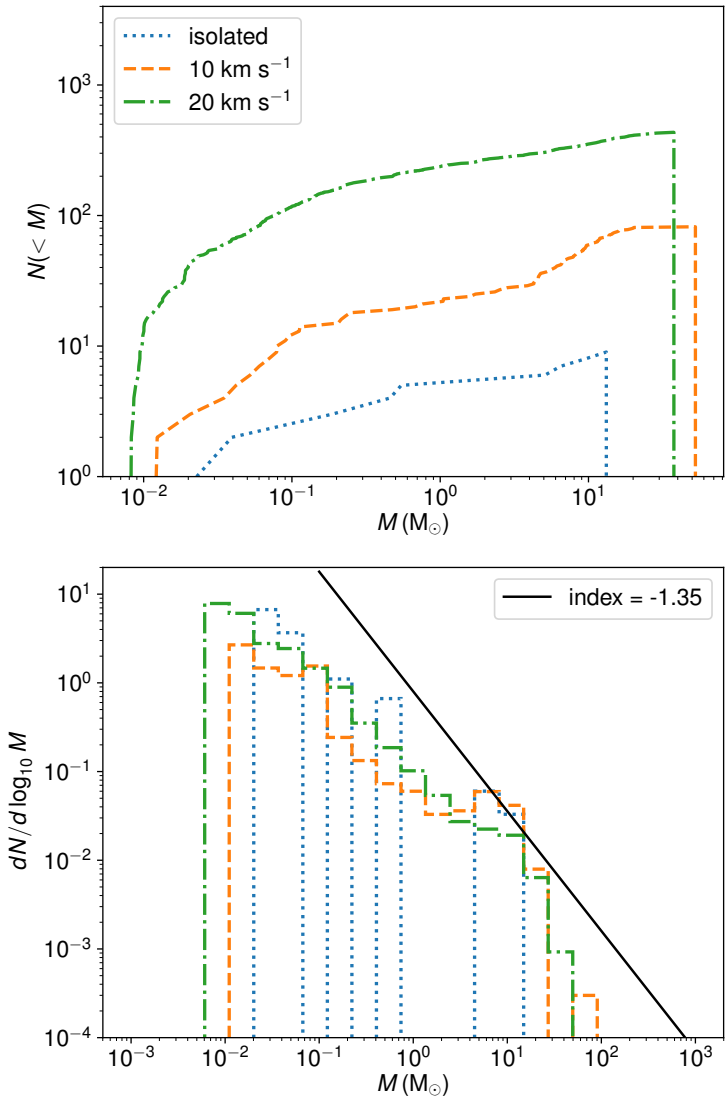

Figure 4.4: The cumulative stellar mass distribution (left) and stellar mass function (right) for the isolated and two colliding cloud cases without photoionising feedback at 4 Myr. Black solid line shows the gradient of the Salpeter IMF.

53 times as rapid. This demonstrates how sensitive the star formation rate is to gas compression (Federrath & Klessen 2012; Federrath et al. 2016). By 6 Myr, the colliding clouds have a SFE of between 10–20%; a factor of 10 higher than the isolated cloud.

Observations of GMCs suggest that the SFE should be of order a few percent (for example, see Table 3 in Federrath & Klessen (2013), which lists the SFE for various clouds in the Milky Way.) This would initially appear to agree better with the isolated cloud than the collision cases. However, true GMCs are typically more extended structures than the idealised Bonnor-Ebert spheres. Real clouds are part of the Galaxy's dynamic ISM and thus subject to turbulent perturbations and tidal interactions that create extended, elongated structures. A cloud collision is therefore likely to involve only part of the cloud. Examples of this can be seen in Fukui et al. (2017), who shows the observational maps of cloud collisions within the LMC or in the numerical simulations of Jin et al. (2017). Collisions are therefore likely to affect a smaller fraction of the cloud's volume than in this idealised case, driving down the total SFE when averages with more quiescent regions.

The resulting star formation can be seen in the cumulative mass in star particles shown in the left-hand panel of Figure 4.4 for the simulations without feedback by 4 Myr. The collisional simulations form more low mass stars and massive star clusters than the isolated case, confirming that turbulence in the collisional shock front also acts as kinetic support to favour the production of massive stars. The largest cluster formed in the isolated cloud is $13\,\mathrm{M}_\odot$, while the collision at $10\,\mathrm{km\,s^{-1}}$ yields a maximum cluster mass of $53\,\mathrm{M}_\odot$ and a slightly lower $38\,\mathrm{M}_\odot$ for the $20\,\mathrm{km\,s^{-1}}$. While the maximum mass is reduced in the faster collision compared to the slower interaction, the total stellar production is greater, with the $20\,\mathrm{km\,s^{-1}}$ creating around five times more sink particles than in the $10\,\mathrm{km\,s^{-1}}$ collision. The smaller size of the maximum mass star cluster is likely due to the faster shock front providing less time to accrete gas, a factor noted by Takahira et al. (2014) as the reason why steadily faster shocks do not form ever larger clumps. By contrast, the isolated cloud case created only 9 sink particles during the first 4 Myr, compared with 83 and 434 in the colliding runs.

The distribution of the stellar masses of the sink particles can be seen in the mass function in the right-hand panel of Figure 4.4 for the same runs. The black solid line in this figure shows a power-law relation with an index of -1.35, which is the prediction of the Salpeter IMF, described by $dN/d\log_{10} M \propto m^{-\chi}$ for $\chi = 1.35$. Since the simulations really only resolve star clusters, the mass function I plot is best interpreted as a molecular core mass function and not as the stellar IMF. Despite significant differences in

the total number of stars and the maximum cluster mass, both the isolated and colliding cloud runs show a similar gradient that is consistent with the slope of the Salpeter IMF. It is worth noting that the isolated cloud has only nine sink particles, so the distribution for this run is relatively scarce. However, the particles formed do appear to follow the same trend as for the colliding cases.

At the high-mass end, the colliding clouds both show extensions beyond the isolated case, indicating the effectiveness of forming high-mass stars during a collision. There is evidence in this region that the IMF may steepen. This fall-off likely corresponds to star formation that occurs only in the densest part of the shock interface.

4.4.3 The Effect of Stellar Feedback

While the cloud collision provides an external source of stirring to the GMC gas, the stars themselves will add energy to their surrounding medium. To explore this, I include photoionising feedback as described in Section 4.2.1 in the isolated cloud simulation and the collisional case at $10\,\mathrm{km\,s^{-1}}$ impact velocity.

The evolution of the star formation efficiency when feedback is included is shown in Figure 4.5. The dashed and dotted lines show the same result for the non-feedback case as in Figure 4.3, with blue-dots showing the result for the isolated cloud and orange-dash and green-dot-dash for the $10\,\mathrm{km\,s^{-1}}$ and $20\,\mathrm{km\,s^{-1}}$ collisional case, respectively. The solid blue line shows the isolated cloud SFE when photoionising feedback is included, while the solid orange and green lines show the feedback results for the colliding clouds. The bottom panel of the figure shows the difference between the equivalent non-feedback and feedback runs, where δ is defined as $\delta(t) = (\mathrm{SFE_{Feedback}(t) - SFE_{NoFeedback}(t)})/\mathrm{SFE_{NoFeedback}(t)} \times 100\%$. A positive value of δ corresponds to feedback promoting the star formation in the cloud, while a negative value means that star formation is being suppressed.

In both the isolated and colliding cases, the effect of feedback is generally to promote star formation over the 6 Myr. This effect was previously seen in Chapter 3 in cases where the feedback had a chance to act before the gas became so dense that the self-gravity dominated over the pressure from the feedback. There, the radiation heated the gas to suppress fragmentation and allowed the gas to be accreted to form more massive stars. This persisted until the cloud was dispersed by the feedback, leading to a subsequent drop in star formation.

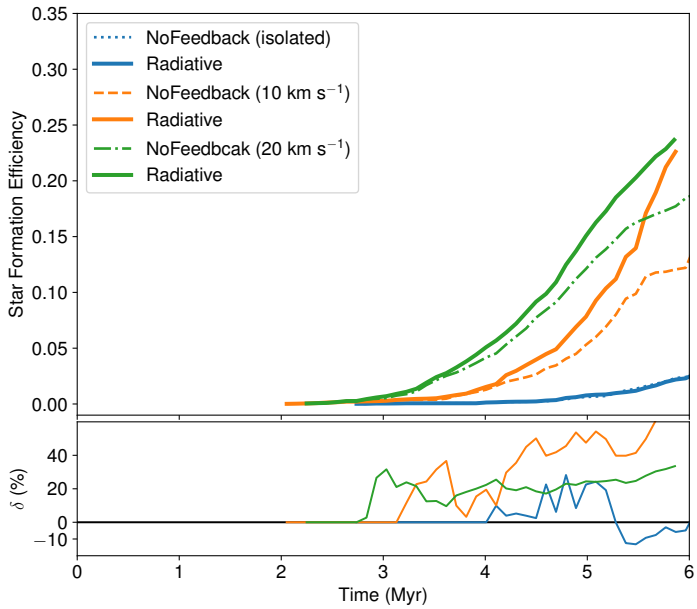

Figure 4.5: Star formation efficiency for the isolated (blue / blue dot-dot), $10\,\mathrm{km\,s^{-1}}$ collision (orange / orange-dash) and $20\,\mathrm{km\,s^{-1}}$ collision simulation (green / green-dot-dash) when photoionising feedback is included. Feedback runs are denoted by the solid lines. The ratio of the difference between non-solid (non-feedback) and solid (feedback) lines are also shown in the lower panel, with a +/- value indicating the positive/negative effect of feedback.

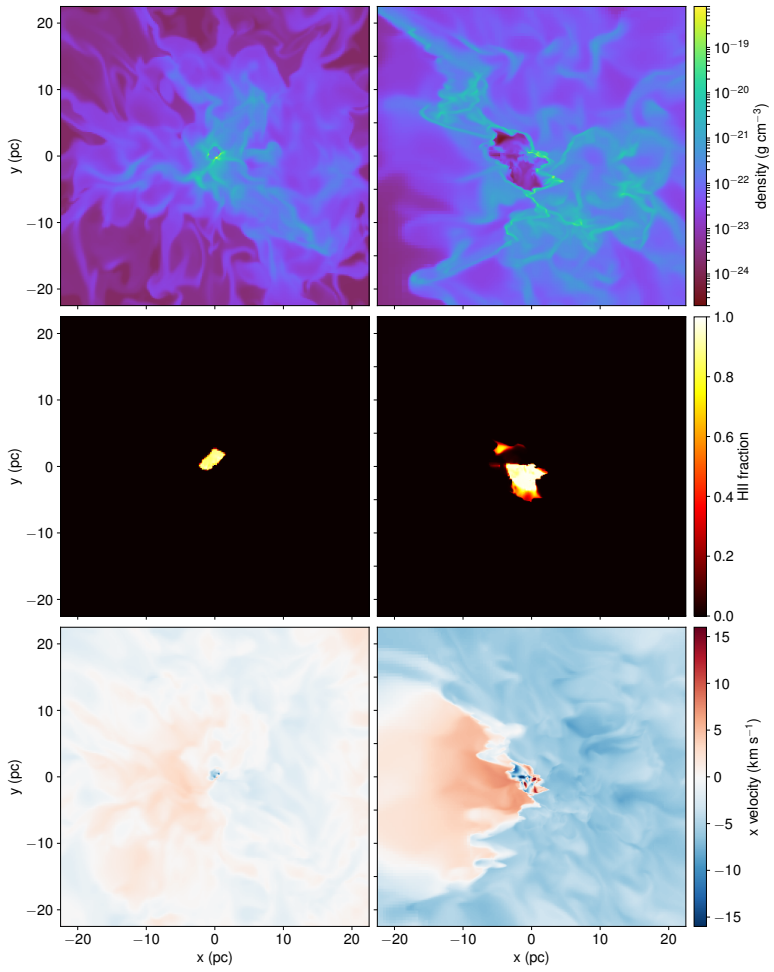

Figure 4.6: The gas density (top), H II fraction (middle), and x-velocity (bottom) on a slice for the feedback runs in the isolated cloud case (left) and 10 km s^{-1} collisional case (right). Images are centered around the most massive sink particle a few Myr after it begins to emit radiation. The isolated cloud is shown at 5.2 Myr, while the colliding case is at 3.7 Myr as the sink formation time differs between these runs. The off-set in the velocity colourbar matches the shock propagation speed in the colliding cloud case of 5 km s^{-1}.

In the isolated cloud, I repeat this effect. Feedback initially makes a positive difference and raises the SFE. As the dense clumps within the cloud begin to be dispersed around 5.5 Myr, the star formation drops compared to the non-feedback case were collapse continues unabated.

When feedback acts during the cloud collision, the effect is uniformly positive, with feedback aiding stellar production. This is from the photoionisation heating of the dense gas within the shocked collisional interface, preventing fragmentation and allowing still larger stars to form. This agrees qualitatively with the smaller-scale simulations of ionising feedback by Peters et al. (2010; 2012), who simulated collapsing molecular cores with radiative feedback and found that the heated gas boosted the Jeans mass to form massive star clusters. While the feedback there could be both positive and negative, it was primarily positive when averaged over longer timescales. This boost in stellar production is stronger in the $10\,\mathrm{km\,s^{-1}}$ case than in the faster $20\,\mathrm{km\,s^{-1}}$ collision. As I will see below, this is due to the speed of the shock front compared to that of the expanding H II region.

Exactly why the feedback can have different effects on the cloud SFE can be seen visually in a close-up image of the gas around the most massive sink particle a few Myr after it has begun to emit radiation in Figure 4.6. The left-hand column of images shows the gas around the massive sink in the isolated cloud case, while the right-hand images shown the collisional case for a velocity of $10\,\mathrm{km\,s^{-1}}$. In the middle row of images showing the H II fraction (H II mass divided by hydrogen mass), a bubble of hot ionised gas can be seen expanding around the photoionising sink. The total H II mass is $0.003\,\mathrm{M_\odot}$ in the isolated cloud case and $6.2\,\mathrm{M_\odot}$ in the collisional case. The top row shows the gas density in a slice at the sink's position, while the bottom row shows the velocity in the direction of the collision. In the collisional case, the velocity axis has been shifted to match the shock propagation speed. As the formation of the sink particles differ between simulations, the isolated case shows the most massive sink forming at 5.2 Myr, while the collisional case is at 3.7 Myr.

The isolated cloud forms its massive stars close to the cloud center, as gas is collapsing towards this region as the initial turbulent support decays. As the massive star cluster forms and begins to photoionise, the radiation heats the surrounding layers of gas and prevents further fragmentation in this region. This suppresses the formation of smaller stars, but allows the gas to be accreted onto the massive star cluster. The mass of the star clusters forming in the simulation therefore increases, as in Chapter 3. Eventually, the heat from the centrally concentrated radiating stars counters the gravitational collapse and further accretion and the star formation begins to slow. This

results in the negative effect we see in Figure 4.5 around 5.5 Myr.

In the case of the colliding clouds, the gas structure is markedly different. The first massive sinks form in the shock generated at the collision interface. As the shock continues to move forward, the H II region expands behind and in front of the shock front. The shock propagation speed for the collision at $10\,\mathrm{km\,s^{-1}}$ is approximately $5\,\mathrm{km\,s^{-1}}$ through the cloud, but with a thermal temperature of $\sim 10^4\,\mathrm{K}$, the maximum expanding velocity due to the pressure gradient is around $10\,\mathrm{km\,s^{-1}}$ corresponding to the sound speed within the H II region. This allows the H II region to stay within the dense gas piling onto the shock front, continuing to suppress fragmentation in this very dense region and allowing the gas to be accreted onto the massive sinks. Since the high density of the shock front is harder to dispel than the gas in the isolated case, feedback continues to have a positive impact on the SFE. This can be seen quantitatively in the mass function for the run in Figure 4.7. The orange solid line corresponds to the simulation with radiation feedback, while the dashed line is for the non-feedback case for the cloud collision at $10\,\mathrm{km\ s^{-1}}$, both taken at 4.5 Myr. The photoionisation results in more high-mass star particles being created as fragmentation into smaller stars is suppressed. While the trend for the stellar mass function for the faster cloud collision at $20\,\mathrm{km\,s^{-1}}$ is the same, the overall effect is more modest. In the bottom panel showing the net effect of feedback on Figure 4.5, the green line is below the orange line. This is again due to the swiftness of the shock front passing through the cloud. With the higher propagation speed, the expanding H II region is outstripped and can have less effect on the star-forming gas. As we have seen, the reduced time of the shock front within the cloud also lowers the maximum mass of the sinks, additionally lowering the impact of the feedback.

Previous simulations have suggested that expanding H II regions could still promote the formation of smaller stars in a 'collect and collapse' scheme, where stars form around the edge of the expanding bubble. However, as in Chapter 3, I find no evidence of that mechanism in play within the simulations, neither within the isolated nor the collisional case.

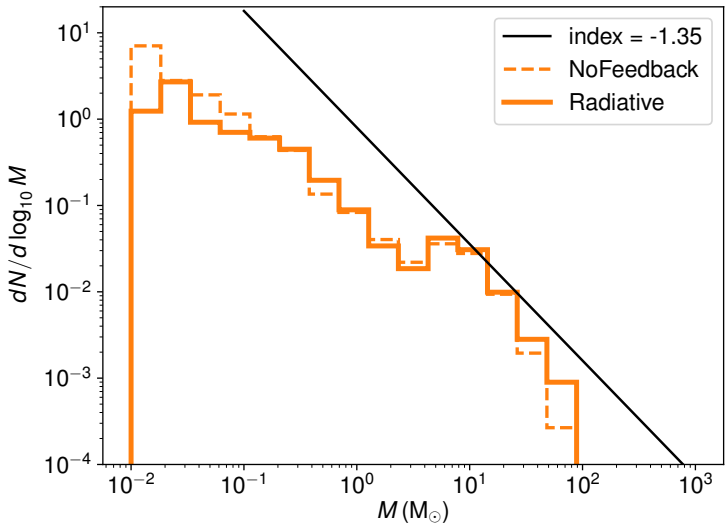

Figure 4.7: Stellar mass function at 4.5 Myr for the $10\,\mathrm{km\,s^{-1}}$ colliding cloud case with and without photoionising feedback.

4.5 Conclusions

I compared stars forming in idealised isolated and colliding cloud cases at two different velocities with a sink particle method for forming stellar clusters and also emitting photoionising radiation. The effect of the cloud collision was to increase the total stellar mass formed and also the maximum size of the star cluster born in the simulation, compared with the isolated cloud case. The collision created a dense shock front and compressed the gas within the colliding clouds. The added density provided a larger reservoir of gas for star formation, while the compressive turbulence promoted the production of more high mass stars. The higher collision velocity increased the total stellar mass due to the production of a denser shock front, but the slower velocity speed produced the highest individual cluster mass and strongest response to feedback, due to the reduced speed increasing the time for the sink particle to accrete. The overall gradient of the stellar mass distribution was not strongly different between the isolated and colliding cases and remains consistent with a Salpeter IMF for star clusters up to $10\,M_{\odot}$. At the higher mass clusters achieved during the cloud collision simulations, the power-law relation appears to steepen. This may suggest that the biggest stellar clusters can only be formed during a collision between clouds and not through regular gravitational collapse. The addition of photoionising feedback affected the isolated and colliding clouds differently, due to differences in the structure of the gas. In both cases, the radiation initially suppressed fragmentation, throttling the production of smaller stars but allowing more gas to be accreted onto the larger star clusters. This created a positive impact on the SFE. In the isolated case, radiation from the centrally concentrated star formation began to counter the gravitational collapse after several Myr. This ultimately slowed the production of stars and throttled the cloud SFE. In the collisional case, the expanding H II region from the massive star clusters was able to keep pace with the shock front as it travelled through the cloud. The particularly dense gas inside the shock front was not dispersed by the radiation, which continued to have a positive impact on the SFE. The overall effect of the collision is therefore to boost the production of high-mass stars. Providing the shock speed is comparable to the sound speed within the resulting H II regions, feedback can be a positive force on star formation triggered in collisions, while it ultimately curtails star formation in the less dense isolated system.

Acknowledgements

I would like to express my gratitude to my mentors Elizabeth Tasker and Asao Habe for their guidance and advice. I also would like to thank Takashi Okamoto for giving me some comments. I greatly appreciate the our laboratory members both in my public and my private life.

Numerical computations were [in part] carried out on Cray XC30 at Center for Computational Astrophysics, National Astronomical Observatory of Japan. Figures are produced by using YT (Turk et al. 2011).

Bibliography

Abel, T., Anninos, P., Zhang, Y., & Norman, M. L. 1997, New Astron., 2, 181

Abel, T., & Wandelt, B. D. 2002, MNRAS, 330, L53

Alves, J. F., Lada, C. J., & Lada, E. A. 2001, Nature, 409, 159

Anninos, P., Zhang, Y., Abel, T., & Norman, M. L. 1997, New Astron., 2, 209

Arzoumanian, D., André, P., Didelon, P., et al. 2011, A&A, 529, L6

Balfour, S. K., Whitworth, A. P., Hubber, D. A., & Jaffa, S. E. 2015, MNRAS, 453, 2471

Balfour, S. K., Whitworth, A. P., & Hubber, D. A. 2017, MNRAS, 465, 3483

Bate, M. R. 2009, MNRAS, 392, 1363

Beaumont, C. N., Offner, S. S. R., Shetty, R., Glover, S. C. O., & Goodman, A. A. 2013, ApJ, 777, 173

Benincasa, S. M., Tasker, E. J., Pudritz, R. E., & Wadsley, J. 2013, ApJ, 776, 23

Bigiel, F., Leroy, A. K., Walter, F., et al. 2011, ApJ, 730, L13

Bonnor, W. B. 1956, MNRAS, 116, 351

Bryan, G. L., Norman, M. L., O'Shea, B. W., et al. 2014, ApJS, 211, 19

Cartwright, A., & Whitworth, A. P. 2004, MNRAS, 348, 589

Chabrier, G. 2005, The Initial Mass Function 50 Years Later, 327, 41

Chomiuk, L., & Povich, M. S. 2011, AJ, 142, 197

Dale, J. E., Ercolano, B., & Bonnell, I. A. 2012, MNRAS, 424, 377

Dale, J. E., Ercolano, B., & Bonnell, I. A. 2012, MNRAS, 427, 2852

Dale, J. E., Ngoumou, J., Ercolano, B., & Bonnell, I. A. 2014, MNRAS, 442, 694

Dobbs, C. L., Burkert, A., & Pringle, J. E. 2011, MNRAS, 413, 2935

Dobbs, C. L., Pringle, J. E., & Duarte-Cabral, A. 2015, MNRAS, 446, 3608

Donovan Meyer, J., Koda, J., Momose, R., et al. 2013, ApJ, 772, 107

Federrath, C., Klessen, R. S., & Schmidt, W. 2008, ApJ, 688, L79

Federrath, C., Banerjee, R., Clark, P. C., & Klessen, R. S. 2010, ApJ, 713, 269

Federrath, C., Roman-Duval, J., Klessen, R. S., Schmidt, W., & Mac Low, M.-M. 2010, A&A, 512, A81

Federrath, C., Sur, S., Schleicher, D. R. G., Banerjee, R., & Klessen, R. S. 2011, ApJ, 731, 62

Federrath, C., & Klessen, R. S. 2012, ApJ, 761, 156

Federrath, C. 2013, MNRAS, 436, 1245

Federrath, C., & Klessen, R. S. 2013, ApJ, 763, 51

Federrath, C., Schrön, M., Banerjee, R., & Klessen, R. S. 2014, ApJ, 790, 128

Federrath, C. 2015, MNRAS, 450, 4035

Federrath, C. 2016, MNRAS, 457, 375

Federrath, C., Rathborne, J. M., Longmore, S. N., et al. 2016, ApJ, 832, 143

Federrath, C., Rathborne, J. M., Longmore, S. N., et al. 2017, The Multi-Messenger Astrophysics of the Galactic Centre, 322, 123

Fujimoto, Y., Tasker, E. J., Wakayama, M., & Habe, A. 2014, MNRAS, 439, 936

Fujimoto, Y., Tasker, E. J., & Habe, A. 2014, MNRAS, 445, L65

Fukui, Y., Torii, K., Ohama, A., et al. 2016, ApJ, 820, 26

Fukui, Y., Torii, K., Hattori, Y., et al. 2017, arXiv:1701.04669

Ferland, G. J., Korista, K. T., Verner, D. A., et al. 1998, PASP, 110, 761

Furukawa, N., Dawson, J. R., Ohama, A., et al. 2009, ApJ, 696, L115

Ginsburg, A., Bressert, E., Bally, J., & Battersby, C. 2012, ApJ, 758, L29

Glover, S. C. O., Federrath, C., Mac Low, M.-M., & Klessen, R. S. 2010, MNRAS, 404, 2

Górski, K. M., Hivon, E., Banday, A. J., et al. 2005, ApJ, 622, 759

Gritschneder, M., Naab, T., Walch, S., Burkert, A., & Heitsch, F. 2009, ApJ, 694, L26

Harper-Clark, E., & Murray, N. 2009, ApJ, 693, 1696

Hennebelle, P., & Chabrier, G. 2009, ApJ, 702, 1428

Hollenbach, D., & McKee, C. F. 1989, ApJ, 342, 306

Hughes, A., Meidt, S. E., Colombo, D., et al. 2013, ApJ, 779, 46

Iliev, I. T., Whalen, D., Mellema, G., et al. 2009, MNRAS, 400, 1283

Jin, K., Salim, D. M., Federrath, C., et al. 2017, MNRAS, 469, 383

Kainulainen, J., Federrath, C., & Henning, T. 2014, Science, 344, 183

Kennicutt, R. C., Jr. 1998, ApJ, 498, 541

Klessen, R. S. 2000, ApJ, 535, 869

Koda, J., Scoville, N., Sawada, T., et al. 2009, ApJ, 700, L132

Koenig, X. P., Leisawitz, D. T., Benford, D. J., et al. 2012, ApJ, 744, 130

Kritsuk, A. G., Norman, M. L., & Wagner, R. 2011, ApJ, 727, L20

Krumholz, M. R., & Tan, J. C. 2007, ApJ, 654, 304

Krumholz, M. R., & Matzner, C. D. 2009, ApJ, 703, 1352

Krumholz, M. R., Cunningham, A. J., Klein, R. I., & McKee, C. F. 2010, ApJ, 713, 1120

Krumholz, M. R., Bate, M. R., Arce, H. G., et al. 2014, Protostars and Planets VI, 243

Lada C. J., Lombaridi M. & Alves J. F. 2010, ApJ, 724, 687

Larson, R. B. 1981, MNRAS, 194, 809

Lopez, L. A., Krumholz, M. R., Bolatto, A. D., Prochaska, J. X., & Ramirez-Ruiz, E. 2011, ApJ, 731, 91

Mac Low, M.-M., Klessen, R. S., Burkert, A., & Smith, M. D. 1998, Physical Review Letters, 80, 2754

McKee, C. F., & Williams, J. P. 1997, ApJ, 476, 144

Meidt, S. E., Schinnerer, E., García-Burillo, S., et al. 2013, ApJ, 779, 45

Meidt, S. E., Hughes, A., Dobbs, C. L., et al. 2015, ApJ, 806, 72

Momose, R., Okumura, S. K., Koda, J., & Sawada, T. 2010, ApJ, 721, 383

Murray, N. 2011, ApJ, 729, 133

Offner, S. S. R., & Krumholz, M. R. 2009, ApJ, 693, 914

Offner, S. S. R., Klein, R. I., McKee, C. F., & Krumholz, M. R. 2009, ApJ, 703, 131

Ohama, A., Dawson, J. R., Furukawa, N., et al. 2010, ApJ, 709, 975

Omukai, K. 2000, ApJ, 534, 809

Pan, H.-A., Fujimoto, Y., Tasker, E. J., et al. 2015, MNRAS, 453, 3082

Pan, H.-A., Fujimoto, Y., Tasker, E. J., et al. 2016, MNRAS, 458, 2443

Peters, T., Banerjee, R., Klessen, R. S., et al. 2010, ApJ, 711, 1017

Peters, T., Klaassen, P. D., Mac Low, M.-M., Klessen, R. S., & Banerjee, R. 2012, ApJ, 760, 91

Rey-Raposo, R., Dobbs, C., & Duarte-Cabral, A. 2015, MNRAS, 446, L46

Ripamonti, E., & Abel, T. 2004, MNRAS, 348, 1019

Rogers, H., & Pittard, J. M. 2013, MNRAS, 431, 1337

Roman-Duval J., Jackson J. M., Heyer M., Rathborne J., Simon R., 2010, ApJ, 723, 492

Sánchez, N., & Alfaro, E. J. 2010, Star Clusters: Basic Galactic Building Blocks Throughout Time and Space, 266, 524

Schaerer, D. 2003, A&A, 397, 527

Schneider, N., André, P., Könyves, V., et al. 2013, ApJ, 766, L17

Shima, K., Tasker, E. J., & Habe, A. 2017, MNRAS, 467, 512

Shima, K., Tasker, E. J., Federrath, C., & Habe, A. 2017, PASJ,

Smith, B., Sigurdsson, S., & Abel, T. 2008, MNRAS, 385, 1443

Stone, J. M., & Norman, M. L. 1992, ApJS, 80, 753

Strömgren, B. 1939, ApJ, 89, 526

Takahira, K., Tasker, E. J., & Habe, A. 2014, ApJ, 792, 63

Tan, J. C. 2000, ApJ, 536, 173

Tasker, E. J., & Tan, J. C. 2009, ApJ, 700, 358

Tasker, E. J. 2011, ApJ, 730, 11

Tasker, E. J., Wadsley, J., & Pudritz, R. 2015, ApJ, 801, 33

Torii, K., Hasegawa, K., Hattori, Y., et al. 2015, ApJ, 806, 7

Truelove, J. K., Klein, R. I., McKee, C. F., et al. 1997, ApJ, 489, L179

Turk, M. J., Smith, B. D., Oishi, J. S., et al. 2011, ApJS, 192, 9

Urban, A., Martel, H., & Evans, N. J., II 2010, ApJ, 710, 1343

Walch, S., Whitworth, A. P., Bisbas, T. G., Wünsch, R., & Hubber, D. A. 2013, MNRAS, 435, 917

Whitworth, A. P., Bhattal, A. S., Chapman, S. J., Disney, M. J., & Turner, J. A. 1994, A&A, 290, 421

Williamson, D. J., Thacker, R. J., Wurster, J., & Gibson, B. K. 2014, MNRAS, 442, 3674

Wise, J. H., & Abel, T. 2011, MNRAS, 414, 3458

Wise, J. H., & Cen, R. 2009, ApJ, 693, 984

Wise, J. H., Abel, T., Turk, M. J., Norman, M. L., & Smith, B. D. 2012, MNRAS, 427, 311

Wu, B., Tan, J. C., Christie, D., et al. 2017, ApJ, 841, 88

Wünsch, R., Dale, J. E., Palouš, J., & Whitworth, A. P. 2010, MNRAS, 407, 1963

Appendix

This capther will describe the basic physics of H II regions and resultes of test simulations performed by *Enzo*.

A Ionisation Front Test

A.1 Strömgren Sphere

Stars with surface temperatures above 20000 K emit UV photons ($\lambda \leq$912 Å) that can ionise hydrogen atoms and create H II regions. Strömgren (1939) considered a point monochromatic ionising photon source in a uniform static gas and performed analytical study of the ionisation front (I-front) for the first time. The I-front expands and halts at a equilibrium radius (so-called Strömgren radius: R_S) where the number of photo-ionisations equals the number of recombinations. To compute the R_S, we consider that the recombination rate is proportional to the product of electron and the H II ion (proton) density,

$$\alpha n_e n_p, \tag{A.1}$$

where α is a recombination coefficient, n_e is a electron number density and n_p is a proton number density. If hydrogen is completely ionised within the Strömgren radius, the electron and proton number densities are equal to the original hydrogen number density ($n_e = n_p = n_{\rm H}$). Recombinations directly to the ground state emits a photon that can be re-absorbed and ionise another hydrogen. Such photons do not affect the total recombination rate. It is therefore a better approximation to exclude them. Recombinations to any excited state ($n \geq 2$) are called Case B recombination and the case B recombination coefficient (α_B) at T $= 10^4$ K (typical temperature of H II regions) is:

$$\alpha_B(\mathrm{T} = 10^4\,\mathrm{K}) = 2.6 \times 10^{-13}\,\mathrm{cm^3\,s^{-1}}. \tag{A.2}$$

Then the total number of case B recombinations within R_S equals to the total number of photon emitted per second ($Q_{\rm H}$),

$$\frac{4}{3}\pi R_S^3 \alpha_B n_{\rm H}^2 = Q_{\rm H} \tag{A.3}$$

and we can get

$$R_S = \left(\frac{3Q_{\rm H}}{4\pi\alpha_B n_{\rm H}^2}\right)^{1/3}. \tag{A.4}$$

A.2 Approach to the Strömgren Radius

This section will describe how the I-front radius ($r_{\rm IF}$) reaches the Strömgren radius. As the I-front increases from $r_{\rm IF}$ to $r_{\rm IF} + dr$ in dt, the number of hydrogen atoms that need to be ionised is $(4\pi r_{\rm IF}^2)dr n_{\rm H}$. This equals the number of ionising photons crossing the I-front boundary in dt,

$$4\pi r_{\rm IF}^2 dr n_{\rm H} = (Q_{\rm H} - \frac{4}{3}\pi r_{\rm IF}^3 \alpha_B n_{\rm H})dt. \tag{A.5}$$

Note that any case B recombination photons can not ionise a hydrogen atom and advance the I-front. By substituting equation (A.3) for $Q_{\rm H}$, the expansion speed of the I-front is given by,

$$\frac{dr}{dt} = \frac{1}{4\pi r_{\rm IF}^2 n_{\rm H}}\left(Q_{\rm H} - \frac{4}{3}\pi r_{\rm IF}^3 \alpha_B n_{\rm H}\right) \tag{A.6}$$

$$= \frac{1}{t_{\rm rec}}\frac{R_S^3}{3r_{\rm IF}^2}\left(1 - \frac{r_{\rm IF}^3}{R_S^3}\right), \tag{A.7}$$

where $t_{\rm rec} = (n_{\rm H}\alpha_B)^{-1}$ is the recombination time. Changing of a variable ($x = (r_{\rm IF}/R_S)^3$) yields,

$$\frac{dx}{1-x} = \frac{dt}{t_{\rm rec}}. \tag{A.8}$$

We can integrate the both side with a initial condition ($x = 0$ at $t = 0$) and get

$$\ln(1-x) = -\frac{t}{t_{\rm rec}}, \tag{A.9}$$

giving

$$r_{\rm IF}(t) = R_S(1 - \exp(-t/t_{\rm rec}))^{1/3}. \tag{A.10}$$

The I-front expand quickly at first and the speed slows down in the recombination time scale. The typical star forming region density $n_{\rm H} \sim 10^2\,{\rm cm}^{-3}$ gives $t_{\rm rec} \sim 10^2\,{\rm yr}$ and the time scale is very short compared to the hydrodynamics time scale. So, the static gas assumption is better approximation.

Table A.1: Strömgren sphere parameters

uniform density	10^2	cm^{-3}
fixed temperature	10^4	K
Stellar luminosity	10^{48}	$\mathrm{ph\,s}^{-1}$
Strömgren radius	1.46	pc
recombination time	1.22×10^3	yr

Table A.2: Simulations performed.

run	root grid	HELPix level (number of rays)
Res32L1	32^3	1 (48)
Res64L1	64^3	1 (48)
Res32L2	32^3	2 (169)

A.3 Initial Condition

I performed 3D test simulations of a expanding I-front in a uniform static gas with a fixed temperature. The simulation box size is 2 pc along each side and a monochromatic photo-ionising source locates at the left-edge corner $(x, y, z) = (0, 0, 0)$. I follow only the evolution in a $x > 0, y > 0, z > 0$ region to reduce the computational cost. The properties of the Strömgren sphere are summarized in Table A.1. I performed three runs with different resolution and number of sampling rays for the HEALPix framework of the adaptive ray-tracing scheme. The conditions are summarized in Table A.2.

A.4 Results

Figure A.1 shows the slice plots at z=0 plane for the expanding I-front test simulation covered by a root grid with 64^3 (Res64L1 in Table A.2) after one recombination time. The top panel shows the H I fraction, while the bottom panel shows the ionisation rate. I defined the I-front as a radius where the H I fraction equals 0.5. The evolution of the I-front radius for each runs is shown in the top panel of Figure A.2. The results with different resolution and number of rays are plotted by different maker (Res32L1: $\times$, Res64L1: $+$, Res32L2: $\circ$). The analytical solution based on equation (A.10) is also plotted by black solid line. The time is normalised by the recombination time. All runs show a good agreement with the analytical solution. The bottom panel of Figure A.2 shows the spherically averaged ionisation rate at $t = t_{\rm rec}$ for the Res32L1 run. The radius is normalized by the Strömgren radius. A slope of r^{-2} is also plotted with black dashed line. The number of

photons absorbed at reach radius is well sampled. I concluded that the resolution with root grid 32^3 (the minimum cell size of 0.0625 pc) and HELPix Level 1 (the number of sampling rays of 48) are enough for modeling the H II region.

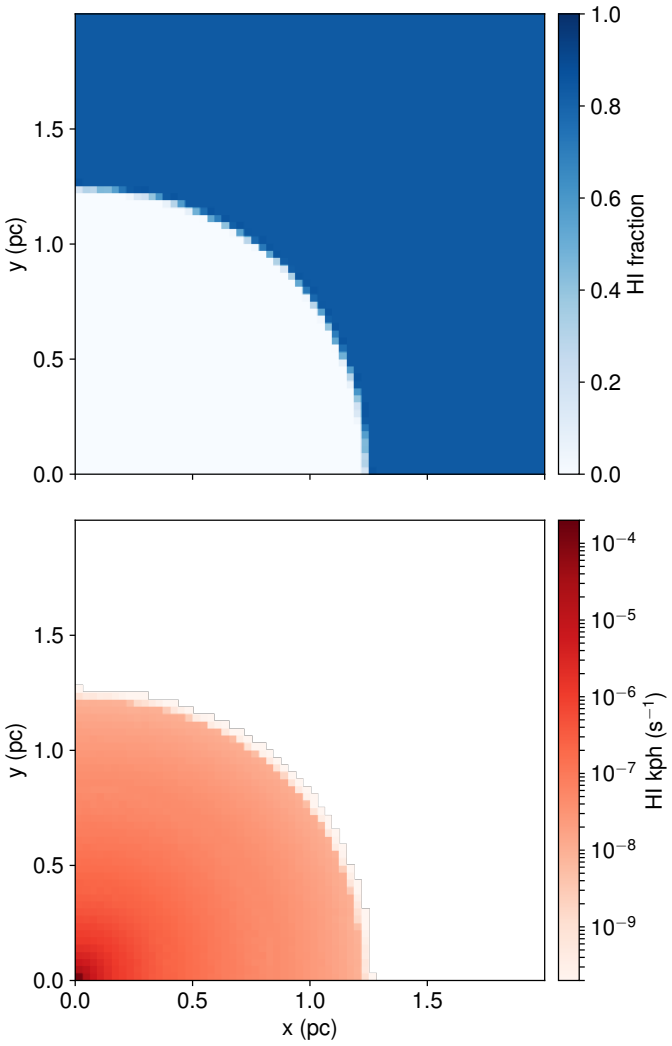

Figure A.1: Slice plots of the H I fraction (top) and the ionisation rate (bottom) at $t = t_{\mathrm{rec}}$ for the Res64L1 run. The source position is (0, 0).

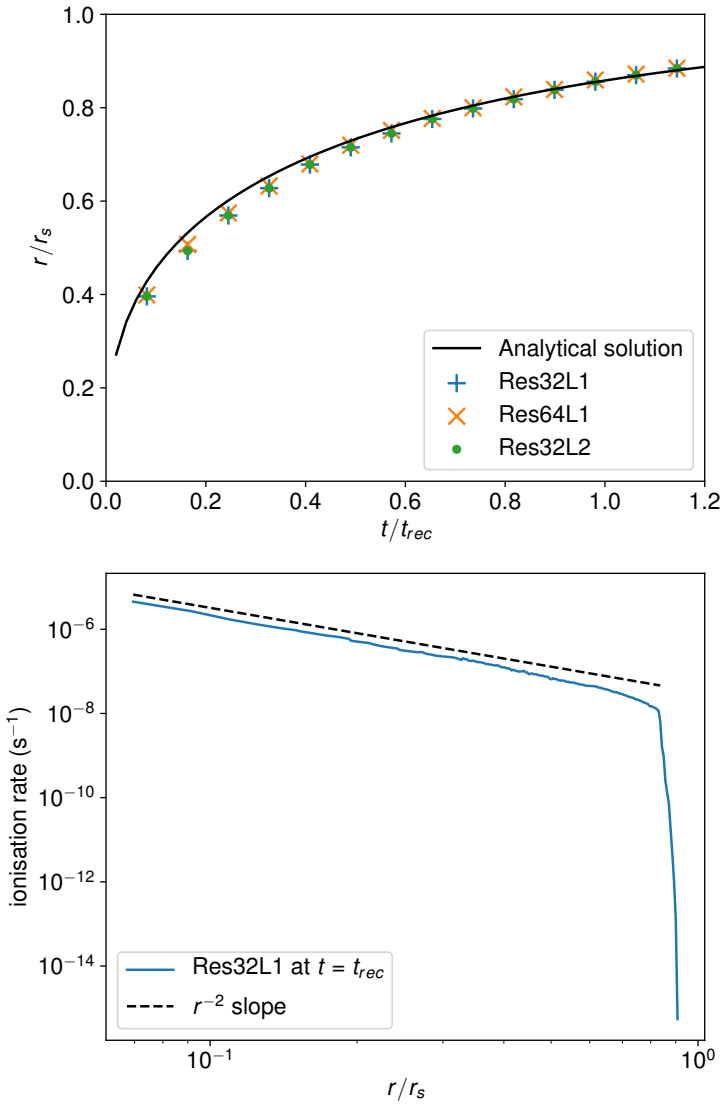

Figure A.2: (top) The evolution of I-front radius as a function of a normalised time by the recombination time for Res32L1 ($\times$), Res64L1 ($+$) and Res32L2 ($\circ$). The black solid line shows the analytical solution. (bottom) The averaged ionisation rate as a function of a normalized radius by the Strömgren radius at $t = t_{\rm rec}$ for the Res32L1 run. The black dashed line shows the slope of r^{-2}.

B Shock Front Test

The previous test was done on a fixed density field because the I-front evolution is very faster than the hydrodynamic response of the gas (R-type I-fronts). As the I-front decelerates and is trapped near the Strömgren radius, the I-front changes to D-type. The ionised gas is much hotter than its neutral environment causing high pressure and rising expansion flows. The expanding flows sweep up gas and create a density shock front (S-front). I performed test simulations of expanding H II region into a r^{-2} density profile. This condition is based on Test6 in Iliev et al. (2009).

B.1 Initial Condition

I performed a 3D test simulation of expanding H II region into a power-law density profile. The simulation box size is 3 pc along each side covered by a root grid with 64^3 cells, with additional two levels of adaptive refinement. A monochromatic photo-ionising source locates at the left-edge corner $(x, y, z) = (0, 0, 0)$. I follow only the evolution in a $x > 0, y > 0, z > 0$ region to reduce the computational cost. The power-law density profile with a flat core is given by,

$$n(r) = \begin{cases} n_0, & \text{if } r \leq r_0 \\ n_0 (r/r_0)^{-2}, & \text{if } r \geq r_0. \end{cases} \tag{B.11}$$

The core density (n_0) and the source properties are the same with the previous test (Table A.1), but the temperature is not fixed. The initial temperature is 100 K. I choose the core radius (r_0) as the Strömgren radius. In this case, the I-front evolves as R-type first and changes to D-type after a few recombination time. I follow the long-term evolution until 50 kyr ($\sim 40 t_{\rm rec}$).

B.2 Results

Figure B.3 shows the density structures at the different stages of the evolution, at t = 10, 20, 30 and 40 kyr. Figure B.4 shows 1D radial profiles averaged spherically for the ionisation fraction (top), density (middle) and temperature (bottom) at t=10 and 40 kyr. The dot-dashed lines in density and temperature plots shows the initial condition. I defined the S-front radius as the peak position of the radial density profile. Figure B.5 shows the evolution of the S-front radius and the propagation speed as a function of a time. I ignore data for first a few kyr because the hydrodynamical response is weak. The shock propagation into a power-law density profile has no analytical solution but it has been studied by numerical. The shock moves

with a roughly constant velocity correspond to the sound speed of ionised gas ($\sim$11 km/s at $T = 10^4$ K and $\mu = 0.6$) and the velocity increased little by little. This is consistent with Iliev et al. (2009).

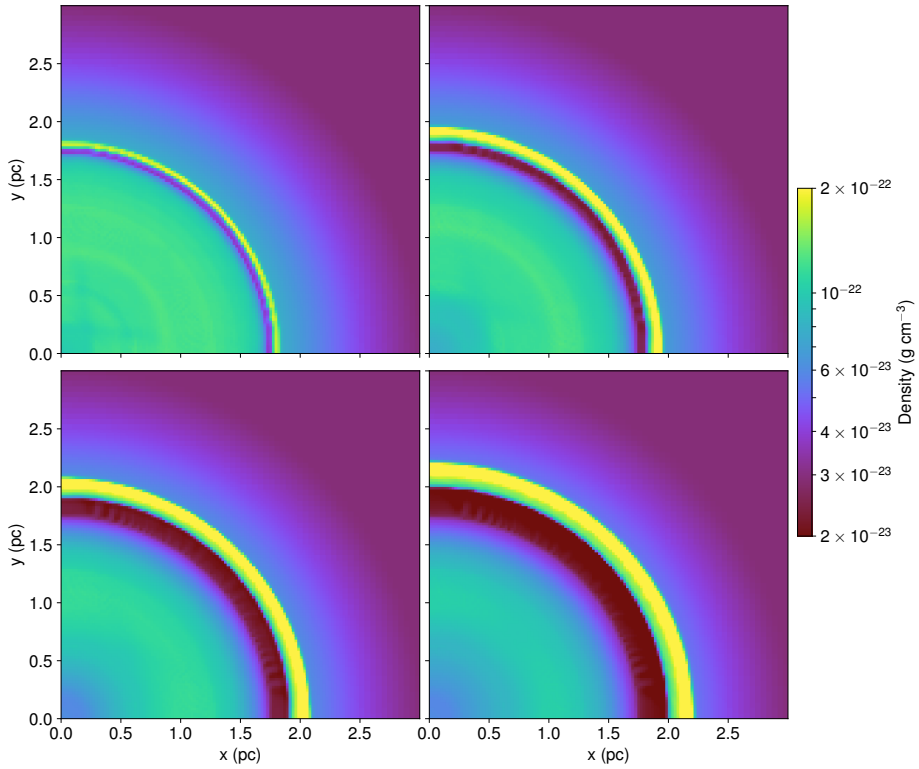

Figure B.3: Comparison of the gas density at different time (top-left: 10, top-right: 20, bottom-left: 30, bottom-right: 40 kyr), at coordinate z=0.

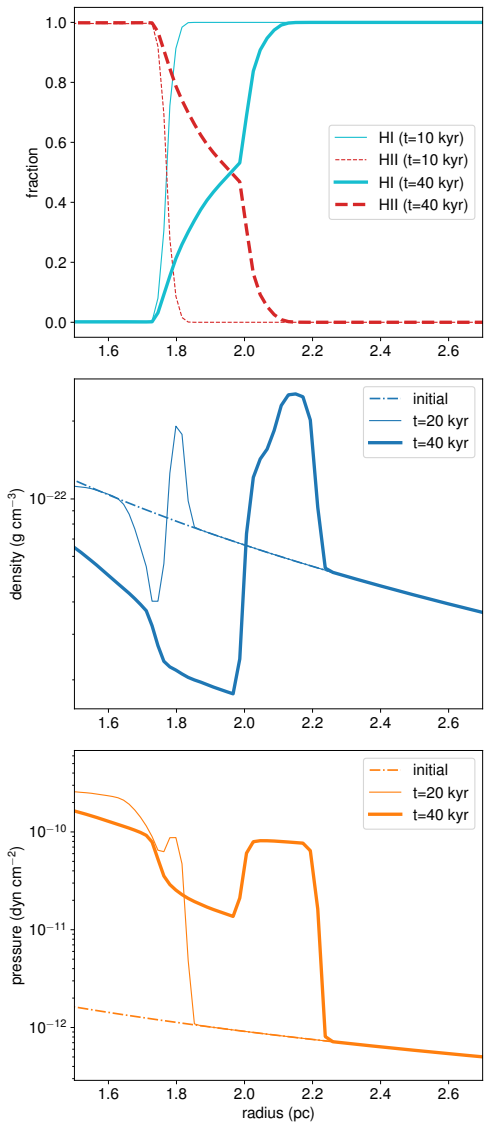

Figure B.4: Spherically averaged profile at 10 and 40 kyr for the H I and H II fraction (top), density (middle), and pressure (bottom). The initial conditions of density and pressure are plotted with dot-dashed lines.

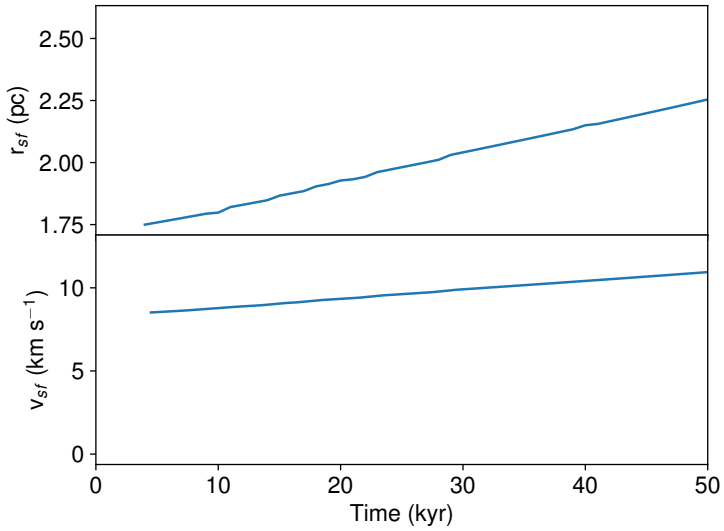

Figure B.5: The evolution of shock front radius (top) and the propagation speed (bottom).